Journal of Volcanology and Geothermal Research 355 (2018) 232–252

Contents lists available at ScienceDirect

Journal of Volcanology and Geothermal Research

journal homepage: www.elsevier.com/locate/jvolgeores

Insights into the petrogenesis of low- and high-Ti basalts: Stratigraphy and geochemistry of four lava sequences from the central Paraná basin

Angelo De Min [a,*], Sara Callegaro [b], Andrea Marzoli [c], Antonio J. Nardy [d], Massimo Chiaradia [e], Leila S. Marques [f], Ilaria Gabbarrini [a]

[a] Department of Mathematics and Geosciences, University of Trieste, Italy
[b] Department of Geosciences, University of Oslo, Norway
[c] Department of Geosciences, University of Padua, Italy
[d] Department of Petrology and Metallogenesis, University of S. Paulo state, Brazil
[e] Department of Earth Sciences, University of Geneva, Switzerland
[f] Department of Geophysics, University of S. Paulo, Brazil

ARTICLE INFO

Article history:
Received 28 July 2016
Received in revised form 11 August 2017
Accepted 23 August 2017
Available online 8 September 2017

Keywords:
Parana' flood basalts
Lava stratigraphy
Carbonatitic metasomatism
Geochemistry
Petrogenesis

ABSTRACT

Lava flow sequences were sampled in the central part of the Paraná basin aiming to verify the time-related evolution of the Paraná basaltic magmatism. It is shown that low- and high-Ti basalts were erupted synchronously. In particular, Esmeralda and Pitanga flows are interlayered, with the former prevailing in the upper part of the sequence. Evidence for synchronously active magma plumbing systems is also supported by mineralogical data, showing signs of mixing between the two groups.

Geochemical data, including Sr-Nd-Pb isotopic compositions are furthermore used to define the mantle source of various low- (Esmeralda and Gramado) and high-Ti (Pitanga and Urubici) magma types. Involvement of a carbonatitic component is proposed for the genesis of the basalts (particularly for the Urubici ones) as suggested by trace element enrichments unrelated to significant isotopic variations. This carbonatitic signature of the mantle source may be conveyed by CO_2-rich metasomatic fluids or melts percolating upwards within the sub-continental lithospheric mantle (SCLM) leading to rapid and selective enrichment of incompatible trace elements. Metasomatism was probably localized at the outskirts of the basin, were Urubici tholeiites and contemporaneous carbonatites were erupted. Geochemical data also suggest the occurrence of significant amounts of crustal contamination in the LTi magmas (mainly in the Gramado and in the late Esmeralda lavas) while crustal assimilation seems negligible in the HTi samples. Globally, a very complex picture arises for the genesis of the Paraná tholeiites, with near-synchronous and geographically coincident flows undergoing significantly different extents of interaction with the crust and tapping different mantle sources.

1. Introduction

Detailed stratigraphic and geochemical data appear particularly important in the study of the Large Igneous Provinces (LIPs), providing information about the time-related evolution of the magma plumbing systems and of their mantle sources. The well dated and mapped continental flood basalts (CFB) of the Paraná basin are an ideal case study for this kind of investigations. Large volumes (exceeding 10^6 km^3; Peate, 1997) of volcanics constituting the Paraná-Etendeka (P-E) province are presently preserved on the South American and African sides of the South Atlantic Ocean. Magmatism of the P-E had a brief emplacement history (within 1.2 Ma; Thiede and Vasconcelos, 2010) at ca. 134 Ma, preceding the opening of the South Atlantic Ocean.

Paraná CFBs were initially divided into two magma-types (Bellieni et al., 1984; Piccirillo et al., 1988, 1990); i) The low-TiO_2 and low-IE (incompatible elements) basalts (LTi, with $TiO_2 < 3.0$ wt%). These rocks are mainly present in the southern Paraná (south of the Rio Uruguay lineament), where the tholeiitic rocks are overlain by voluminous acid flows; and ii) the high-TiO_2 and IE-rich basalts (HTi, with $TiO_2 > 3.0$ wt%), mainly occurring in the northern Paraná (north of the Rio Piquiri lineament; Fig. 1). Products pertaining to both the HTi and the LTi basalts overlap within the central Paraná basin (Piccirillo et al., 1988, 1990).

Peate et al. (1992) completed a thorough geochemical and stratigraphic study of this LIP, tracking the extension of both low- and high-Ti products, and defining magma groups by means of geochemical and stratigraphic criteria. Thus, all the basalts were further divided into six

* Corresponding author at: Department of Mathematics and Geosciences, University of Trieste, Italy.
E-mail address: demin@units.it (A. De Min).

http://dx.doi.org/10.1016/j.jvolgeores.2017.08.009
0377-0273/

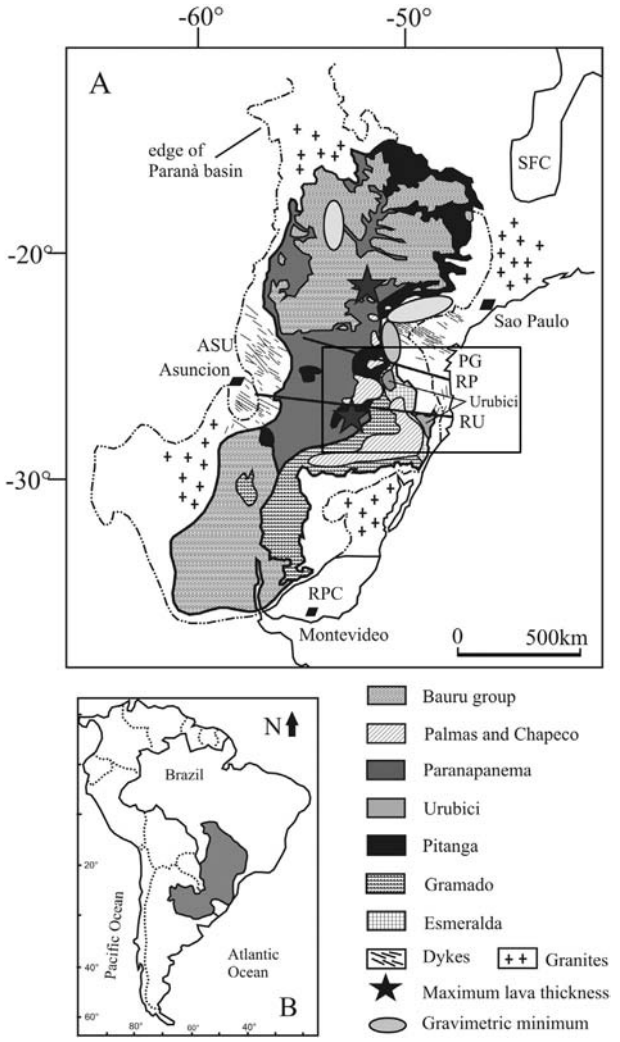

Fig. 1. A: Geological sketch map of the Paraná basin (modified from Thiede and Vasconcelos, 2010). SFC = São Francisco craton; RPC = Rio de la Plata craton; PG = Ponta Grossa dyke swarms; ASU = K-alkaline dyke swarms of the Asuncion-Sapucai graben province (Comin-Chiaramonti et al., 1997); RP = Rio Piquri lineament; RU = Rio Uruguay lineament. The square represents the investigated area. B: Geographic location of the Paraná igneous province sensu stricto in the South American continent.

sub-groups: the LTi Gramado, Esmeralda and Ribeira magma types (north Paraná), and the HTi Urubici, Pitanga and Paranapanema groups (south Paraná; Peate et al., 1992). The acid rocks were grouped into Palmas (LTi) and Chapecó (HTi) magma types (Comin-Chiaramonti et al., 1988).

It is still debated whether the origin of the Paraná LIP is related to a mantle source located within the SCLM (sub-continental lithospheric mantle) or to a mantle plume carrying subduction-related material. The enriched signature of P-E magmas was attributed to a deep plume able to entrain subducted and/or more depleted material at the transition zone (e.g. Ewart et al., 2004) or at the core-mantle boundary (Hoernle et al., 2015). Other authors invoked the involvement of the SCLM (e.g. Hawkesworth et al., 1984, 1988; Piccirillo and Melfi, 1988; Anderson, 1994; Gibson et al., 1995; Peate and Hawkesworth, 1996; Comin-Chiaramonti et al., 1997; Foulger and Natland, 2003; Rosset et al., 2007; Rocha-Júnior et al., 2013). The main difficulty of the latter hypothesis concerns the origin of the heat necessary to readily melt the SCLM in the absence of a mantle plume. In this sense, alternative scenarios have been proposed, such as thermal insulation under mega-continents (Coltice et al., 2007) or fluxing of considerable amounts of metasomatic melts or fluids (water or CO_2) which would lower the peridotite solidus. However, in turn, mobilization of these fluids and melts requires a heat source that probably only an asthenospheric rise or a deep plume system can provide (cf. Mattielli et al., 1999). Further complexities for the understanding of the petrogenesis of the P-E arise from the strong overprint given by secondary processes (such as crustal contamination) that seem to play a prominent role.

This contribution is focused on the Paraná, the South American portion of the P-E LIP. We here present a new stratigraphic study of 4 lava piles from the Paraná basin, and crystal and whole-rock geochemical data on 54 samples. With these new data, we aim to contribute to the study of the temporal and petrologic relationships between low- and high-Ti magmatism (Gramado and Esmeralda vs. Urubici and Pitanga types) and to further constrain some features that are still debated, such as the role of crustal contamination and metasomatism in the genesis of these magmas.

2. Geological outline

The intra-cratonic Paraná basin is set in central-eastern South America, among Brazil, Uruguay, Paraguay, and Argentina, between the São Francisco and the Rio de la Plata cratons (North and South, respectively). It developed with a NE-SW direction since late Proterozoic times after the Brasiliano orogenic Cycle (700–600 Ma; Melfi et al., 1988), which generated the granitic complexes of the Serra do Mar bordering the basin to the East (Mantiqueira system; da Silva et al., 2005). The subsidence of the basin was particularly important in the Paleozoic and continued in the Mesozoic. During the Early Cretaceous, the basin became the principal center for the basaltic flows emission of the P-E (Fig. 1) large igneous province (LIP; Bryan and Ernst, 2008). These products were locally known as Serra Geral Formation (SGF). Just before, then during and shortly after the Paraná tholeiitic event (from the upper Jurassic to the end of the Cretaceous), the basin edges were seat of alkaline (sodic, potassic) and carbonatitic magmatic activity. This seems to indicate a temporal continuity of the thermal event(s) or, as suggested by several authors, the persistence of a mantle plume-hotspot system (e.g. Turner et al., 1996; Ewart et al., 2004).

Notably, the Paraná basin is not yet in isostatic equilibrium and the Bouguer gravity map shows broad gravity lows (up to −100 mGal) with respect to the basin edges. The basin shows relatively high gravity values (around −50 mGal) along the Paraná River topographic low, corresponding to the maximum lava thickness (Vidotti et al., 1998; Mariani et al., 2013). In comparison, the gravity lows are not coincident with the minimal lava thickness or with the maximum sediment thickness.

The magmatic rocks of the Paraná, mainly represented by quite evolved tholeiitic basalts (>90% in volume) and minor intermediate and acid products (dacites and rhyolites; Piccirillo et al., 1988; Peate et al., 1992), cover about 70% of the Paraná basin, with a surface area of 1.2×10^6 km^2 (Bellieni et al., 1984; Piccirillo et al., 1988; Peate et al., 1992) and reach their maximum thickness (>1.5 km) in the North of the basin. The flows were emplaced over the Botucatu Formation (late Paleozoic to Jurassic continental aeolian red sandstones) and were then overlain by the Aeolian sandstones of the Bauru Group (Late Cretaceous) suggesting a stability of the local climate conditions before and after the Paraná magmatic event.

U-Pb ages for felsic rocks (134.3 ± 0.8 Ma; Janasi et al., 2011) are consistent with the brief peak activity for the Paraná constrained by precise $^{40}Ar/^{39}Ar$ ages on the basaltic rocks (peak age at 134.7 ± 1.0 Ma Thiede and Vasconcelos, 2010; see also Renne et al., 1992, 1996; Marzoli et al., 1999; ages recalculated after Renne et al., 2010, 2011).

Widespread sills, located mainly in the northern Paraná, and basaltic and andesitic dyke swarms are associated with the flows (Piccirillo et al., 1990). The main dyke swarms, i.e. in the Asunción-Sapucai graben in Paraguay and in the Ponta Grossa Arch in Brazil mainly show NW-SE direction. Other dike swarms (NNE-SSW oriented) are parallel to the coast (Santos-Rio de Janeiro and Florianopolis dyke swarms).

Finally, alkaline carbonatitic complexes cropping out at the basin edges (e.g. Jacupiranga and Anitápolis in Brazil or Sapucai in Paraguay; Comin-Chiaramonti and Gomes, 2005; Comin-Chiaramonti et al., 2007a; Gomes et al., 2011) show $^{40}Ar/^{39}Ar$ ages comparable with those of the widespread tholeiitic products (130–135 Ma; Comin-Chiaramonti et al., 2007b, ages recalculated after Renne et al., 2010, 2011).

3. Material and methods

3.1. Sampling

In this study, four lava piles cropping out in the Central-South Paraná basin (Brazil) were sampled flow by flow and, in order to limit the effects of alteration, a strong sample selection occurred directly in the field for each flow unit. The first (Faxinal do Céu, Paraná state, 25.96°S; 51.61°W; hereinafter marked as FC) and the second sequence (2 km north of Trevo, Santa Catarina state, 26.98°S; 52.65°W; hereinafter marked as QI) are spaced about 150 km from one another. These sampling sites are close to the boreholes RS, GO, and SE studied by Peate et al. (1992) to define the chemical stratigraphy of the lava piles in the area. In particular, the first stratigraphic sequence (FC) crops out at 700 to 1100 m above sea level (a.s.l.) and is placed between the RS and GO boreholes. At FC, eight basaltic lava flows samples were collected from what appear to be pahoehoe lobes. The second sequence (QI; 300–700 m a.s.l.) is placed between the GO and SE sequences (Fig. 2), and consists of 12 massive lava flows (all sampled) and interlayered pahoehoe lobes. The thickness of the flows observed in FC and QI sequences ranges from 3 to 20–25 m, with prevalent thicknesses being 3–7 m and 10–15 m, respectively.

The third sequence crops out in the Bom Jardim da Serra area (28.36°S; 49.57°W, Santa Catarina State; hereinafter marked as BJ) on the escarpment of the Serra Geral mountain range and is located at about 300 km from the FC and QI sites (Fig. 2). The samples were collected on the two opposite slopes of the Serra Geral escarpment (named BJ1 and BJ2). A total of thirty-two flows were recognized in the two lava piles. One flow in BJ1 appeared remarkably thinner and more vesicular than the others. We sampled six flows from the BJ1 escarpment and twenty-six from BJ2. The prevailing thickness range for the flows in BJ1 and BJ2 is between 20 and 30 m. Rare thin flows (3–10 m) were found and a few occasionally reach 50 m. Detailed stratigraphic correlations are presented in Fig. 3.

3.2. Analytical techniques

The mineral compositions from 21 rock samples was obtained by electron microprobe analyses (CAMECA SX50 at the CNR-IGG, Padova, Italy), operating at accelerating voltage of 15 kV and beam current of 10 nA, with 20–40 s acquisition times. Routine ZAF (Z–atomic number; A–absorption; F–fluorescence) on-line data reduction and matrix correction procedures were applied. The size of the analytical spot is of

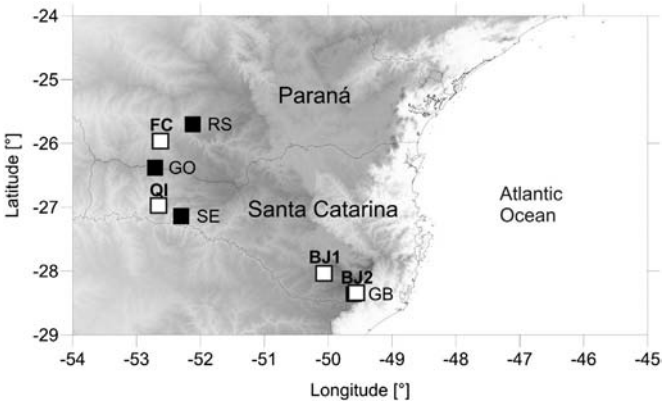

Fig. 2. Location of the boreholes RS, GO and SE and the road profile GB (Mantovani et al., 1988; Peate et al., 1992, 1999) and the new sampling sites FC, QI, BJ1 and BJ2.

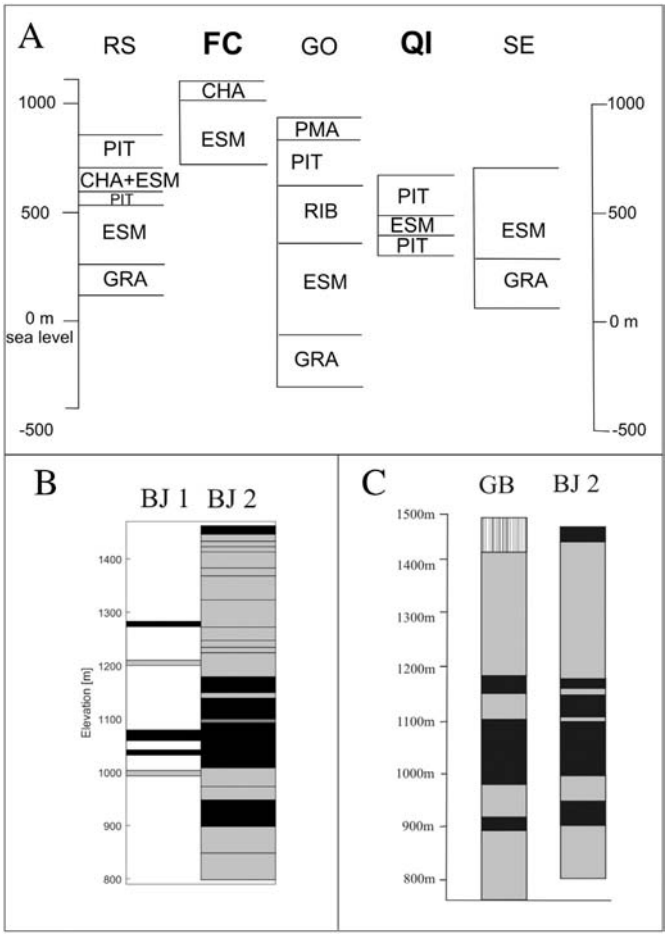

Fig. 3. A: comparison between the boreholes RS, GO and SE stratigraphy and the FC and QI stratigraphic profiles along the schematic N-S section (52°W) modified from Peate et al., 1992. PIT = Pitanga; ESM = Esmeralda; GRA = Gramado; PMA = Paranapanema; RIB = Ribeira; CHA = Chapecó. B: stratigraphic columns of the lava pile in the Sao Joaquim area (BJ). C: comparison between the GB road profile (Peate et al., 1999) and the BJ2 sequence. Grey = LTi basalts Gramado type; Black = HTi basalts Urubici type; White = sediments, vegetation and laterites found between the lava piles. Vertical dashed lines = LTi Palmas type rhyolites.

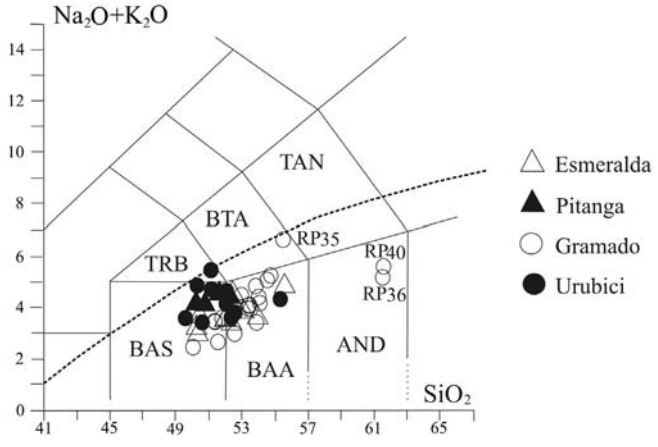

Fig. 4. Distribution of the samples in the TAS diagram (Total Alkali vs. Silica, Le Bas et al., 1986). The dashed line divides the diagram into alkaline and subalkaline fields (Miyashiro, 1978). BAS = basalt; TRB = trachy-basalt; BAA = basaltic andesite; BTA = basaltic trachy-andesite; AND = andesite; TAN = trachy-andesite.

ca. 1 μm. Core to rim compositional profiles on selected plagioclase and pyroxenes crystals were performed.

Whole-rock major element compositions were determined by X-ray fluorescence (XRF) at the University of Padova with a Philips PW2400 spectrometer, following methods described in Callegaro et al. (2013). Analytical uncertainties range from 1% to 2% for major elements.

Trace elements were analyzed by Inductively Coupled Plasma–Mass Spectrometry (ICP-MS) at the University of Bretagne Occidentale at Brest (France) and at the commercial ACMELAB laboratory (Vancouver, Canada), following analytical protocols described in Barrat et al. (1996). A mixture of concentrated HNO_3-HF was added to ca. 100 mg of rock powder in Teflon beakers, and evaporated to dryness at 90 °C. A second evaporation to dryness followed, after addition of ~1–2 ml of concentrated HNO_3. Dry residues were then dissolved in 6 N HCl for archiving. An aliquot of 1 ml of this archive solution was collected and ~5 ng of Tm were added to each sample, and then evaporated to dryness on a hot plate. Samples were finally taken up in HNO_3 2.5% for analysis on the ICP-MS. Geological reference materials of BCR-2 and BIR-1 (US Geological Survey) were used as standards. Difference between certified and published values is <5%.

Radiogenic isotope ratios of Sr ($^{87}Sr/^{86}Sr$), Nd ($^{143}Nd/^{144}Nd$) and Pb ($^{206}Pb/^{204}Pb$, $^{207}Pb/^{204}Pb$, $^{208}Pb/^{204}Pb$) were measured at the Department of Earth Sciences (University of Geneva, Switzerland). The method is described in detail in Chiaradia et al. (2011) and Beguelin et al. (2015). Between 100 and 120 mg of whole rock powder were dissolved during 7 days in Savillex® Teflon vials using 4 ml of concentrated HF and 1 ml of HNO_3 14 M, at a temperature of 140 °C and with the help of ultrasonication for 30 min twice a day. Subsequently, samples were dried and re-dissolved for 3 days (also with 30 min ultrasonication twice a day) in 3 ml of HNO_3 14 M and dried again. Sr, Nd and Pb were then separated using cascade columns with Sr-Spec, TRU-Spec and Ln-Spec resins according to a protocol modified from Pin et al.

Table 1
List of the all samples classified following Peate et al. (1992), elevation and La/Yb and Sm/Yb ratios. Esm = Esmeralda; Pit = Pitanga; Gra = Gramado; Uru = Urubici.

Sample	Type	m asl	SiO_2	TiO_2	P_2O_5	FeOt	Sr	Ba	Zr	Ti/Zr	Ti/Y	Zr/Y	Sr/Y	Ba/Y	La/Yb	Sm/Yb
RP1	Esm	985	53.00	1.72	0.18	14.73	155.12	225.49	153.00	67.39	261.66	3.87	3.93	5.71	4.35	1.38
RP2	Esm	988	52.65	1.78	0.19	15.25	146.00	323.00	156.00	68.40	248.17	3.63	3.40	7.51		
RP3	Esm	937	55.17	1.85	0.28	15.00	165.44	309.99	184.00	60.28	225.87	3.76	3.38	6.33	6.35	1.55
RP4	Esm	1130	50.16	1.33	0.12	12.94	174.00	160.00	81.00	98.44	284.76	2.89	6.21	5.71		
RP5	Esm	1071	52.16	1.46	0.16	14.01	155.20	193.00	131.00	66.81	316.53	4.06	5.62	6.99	4.46	1.38
RP6	Esm	1006	52.75	1.79	0.18	14.74	186.44	278.88	162.00	66.24	243.62	3.66	4.21	6.30	4.91	1.53
RP7	Esm		53.59	1.81	0.21	15.53	155.00	341.00	173.00	62.72	264.66	4.22	3.78	8.32		
RP8	Esm	933	52.07	1.58	0.16	14.36	192.09	216.12	132.00	71.76	228.01	3.17	4.61	5.19	4.04	1.39
RP9	Esm	881	51.72	1.29	0.13	12.75	188.63	203.57	116.00	66.67	264.07	3.96	6.45	6.96	4.79	1.51
RP10	Esm	815	52.20	2.35	0.26	17.07	220.26	395.79	197.00	71.51	240.89	3.36	3.76	6.75	5.55	1.55
RP11	Esm		52.21	2.30	0.26	17.27	185.33	389.21	202.00	68.26	152.33	2.22	2.03	4.27	5.50	1.59
RP12	Esm	759	51.73	2.33	0.26	17.41	188.00	470.00	211.00	66.20	279.37	4.22	3.76	9.40		
RP13	Pit	696	50.03	3.33	0.39	15.47	509.87	497.88	236.00	84.59	483.35	5.73	12.37	12.08	11.22	2.64
RP14	Pit	639	50.02	3.44	0.47	16.38	468.60	532.82	270.00	76.30	442.16	5.78	10.03	11.40	11.08	2.59
RP15	Pit	638	50.52	3.47	0.48	15.91	420.40	495.00	283.00	73.51	653.84	7.58	13.22	15.57	11.56	2.58
RP16	Pit	640	49.88	3.31	0.43	15.73	499.18	502.26	249.00	79.69	456.52	5.71	11.45	11.53	11.11	2.62
RP17	Pit	543	51.98	3.93	0.48	15.07	447.00	736.00	293.00	80.41	199.66	2.48	3.79	6.24		
RP18	Pit	531	51.43	3.95	0.50	14.85	449.40	431.00	298.00	79.46	562.10	6.03	10.65	10.21	9.76	2.86
RP19	Esm	472	50.12	1.59	0.15	14.75	172.27	107.09	100.00	95.32	291.68	3.06	5.28	3.28	2.72	1.33
RP20	Esm	448	50.02	1.60	0.15	15.82	170.23	159.25	121.00	79.27	238.13	2.99	4.21	3.94	3.36	1.36
RP21	Pit	344	51.19	3.47	0.48	15.55	476.54	544.18	271.00	76.76	448.61	5.86	10.30	11.76	11.33	2.63
RP22	Pit	326	50.87	3.48	0.48	15.55	487.56	564.77	278.00	75.05	426.42	5.68	9.96	11.54	11.13	2.60
RP23	Gra	993	52.99	1.15	0.13	11.94	185.40	196.00	123.00	56.05	331.43	3.97	8.96	9.47	5.85	1.53
RP24	Uru	1032	51.70	4.00	0.51	13.62	793.35	612.06	323.00	74.24	518.09	7.00	17.18	13.26	14.24	3.56
RP25	Uru	1059	52.08	3.98	0.52	13.12	1020.00	787.00	308.00	77.47	596.50	7.70	25.50	19.68		
RP26	Uru		51.68	3.71	0.47	13.80	947.94	610.24	299.00	74.39	582.37	7.86	24.93	16.05	15.46	3.82
RP27	Gra	1200	52.60	1.79	0.27	14.07	330.82	495.97	207.00	51.84	252.77	4.88	7.80	11.70	8.57	1.87
RP28	Uru	1273	50.19	3.76	0.53	14.95	501.20	534.00	291.00	77.46	726.91	8.02	16.12	17.17	13.51	3.15
RP29	Uru	1425	50.92	4.32	0.50	14.47	995.97	659.68	329.00	78.72	705.27	9.04	27.37	18.13	16.87	4.10
RP30	Uru	967	50.09	4.25	0.50	14.42	842.00	858.00	329.00	77.44	688.61	8.89	22.76	23.19		
RP31	Gra	1380	53.59	1.45	0.17	13.35	224.02	234.73	149.00	58.34	264.83	4.56	6.86	7.18	6.35	1.73
RP32	Gra	1362	52.84	1.42	0.18	13.24	214.00	377.00	146.00	58.31	257.97	4.42	6.48	11.42		
RP33	Gra	1356	51.10	1.39	0.18	13.63	220.18	249.71	124.00	67.20	275.59	4.08	7.24	8.21	6.17	1.67
RP34	Gra	1346	54.40	1.47	0.18	12.94	174.00	455.00	161.00	54.74	244.80	4.47	4.83	12.64		
RP35	Gra	1331	55.43	1.88	0.29	13.23	119.92	688.78	250.00	45.08	227.21	5.05	2.42	13.93	9.28	1.93
RP36	Gra	1188	61.07	1.42	0.25	9.90	192.42	578.12	232.00	36.69	181.48	4.91	4.07	12.24	10.52	2.04
RP37	Gra	1249	53.12	1.67	0.23	13.84	259.01	408.92	183.00	54.71	293.45	5.40	7.64	12.06	8.25	1.87
RP38	Gra	1210	52.40	1.80	0.27	14.03	322.00	531.00	209.00	51.63	269.78	5.23	8.05	13.28		
RP39	Gra	1194	51.50	1.35	0.17	12.62	211.00	466.00	133.00	60.85	269.78	4.43	7.03	15.53		
RP40	Gra	1180	61.13	1.43	0.27	9.98	173.30	508.00	547.00	34.71	270.36	6.41	5.74	16.03	10.98	2.27
RP41	Gra	1157	49.80	1.00	0.11	10.69	192.00	227.00	87.00	68.91	260.65	3.78	8.35	9.87		
RP42	Gra	1109	53.14	1.82	0.24	13.62	292.84	346.52	178.00	61.30	324.20	5.27	8.66	10.25	7.56	1.95
RP43	Gra		54.24	1.81	0.24	13.94	198.54	388.80	191.00	56.81	304.72	5.37	5.58	10.93	7.75	1.90
RP44	Uru	1111	49.39	4.02	0.51	14.28	781.00	576.00	312.00	77.24	789.67	8.75	25.44	18.76	16.62	3.84
RP45	Uru	1108	50.36	3.97	0.49	13.74	927.44	634.10	305.00	78.03	556.21	7.13	21.69	14.83	15.86	3.73
RP46	Gra	1088	53.52	1.96	0.24	15.20	182.10	323.10	202.00	58.17	241.81	4.16	3.75	6.66	6.52	1.67
RP47	Uru	1092	50.83	4.07	0.51	13.57	634.16	594.93	323.00	75.54	632.48	8.39	16.46	15.44	14.95	3.80
RP48	Uru	1040	50.59	3.89	0.47	13.54	748.00	807.00	323.00	72.20	597.96	8.28	19.18	20.69		
RP49	Uru	1024	51.72	3.98	0.50	13.66	834.97	638.28	306.00	77.97	633.11	8.11	22.14	16.93	15.36	3.85
RP50	Gra	964	52.20	0.98	0.11	11.04	202.00	262.00	105.00	55.95	244.80	4.38	8.42	10.92		
RP51	Gra	935	51.50	0.92	0.09	10.77	314.40	179.00	92.00	59.95	330.99	4.44	18.83	10.72	6.17	1.62
RP52	Uru		54.94	3.55	0.44	11.85	602.30	583.00	287.00	74.15	737.74	9.08	20.84	20.17	14.52	3.64
RP53	Gra	833	53.63	1.40	0.19	12.61	232.00	501.00	185.00	45.37	233.14	5.14	6.44	13.92		
RP54	Gra	811	53.66	1.32	0.18	12.46	216.50	417.00	175.00	45.22	281.66	5.56	7.73	14.89	8.49	1.84

(1994). Finally, the material was redissolved in 2% HNO_3 solutions and ratios were measured using a Thermo Neptune PLUS Multi-Collector ICP-MS in static mode. Ratios used to monitor internal fractionation were: $^{88}Sr/^{86}Sr = 8.375209$ for the $^{87}Sr/^{86}Sr$ ratio, $^{146}Nd/^{144}Nd = 0.7219$ for the $^{143}Nd/^{144}Nd$ ratio and $^{203}Tl/^{205}Tl = 0.418922$ for the three Pb ratios (a Tl standard was added to the solution). Used external standards were SRM987 ($^{87}Sr/^{86}Sr = 0.710248$, long-term external reproducibility: 10 ppm), JNdi-1 ($^{143}Nd/^{144}Nd = 0.512115$; Tanaka et al., 2000; long-term external reproducibility: 10 ppm), and SRM981 (Baker et al., 2004) for Pb (long-term external reproducibility of 0.0048% for $^{206}Pb/^{204}Pb$, 0.0049% for $^{207}Pb/^{204}Pb$ and 0.0062% for $^{208}Pb/^{204}Pb$). $^{87}Sr/^{86}Sr$, $^{143}Nd/^{144}Nd$ and Pb isotope ratios were further corrected for external fractionation (due to a systematic difference between measured and accepted standard ratios) by a value of −0.039‰, +0.047‰ and +0.5‰ amu respectively. Interferences at masses 84 (^{84}Kr), 86 (^{86}Kr) and 87 (^{87}Rb) were corrected by monitoring ^{83}Kr and ^{85}Rb, ^{144}Sm interference on ^{144}Nd was monitored on the mass ^{147}Sm and corrected by using a $^{144}Sm/^{147}Sm$ value of 0.206700 and ^{204}Hg interference on ^{204}Pb was corrected by monitoring ^{202}Hg. Total procedural blanks were <500 pg for Pb and <100 pg for Sr and Nd which are insignificant compared to the amounts of these elements purified from the whole rock samples investigated.

4. Results

4.1. Magma type classification

All the lava flows samples were classified according to the TAS diagram (Fig. 4; Total Alkali vs. Silica; Le Bas et al., 1986) and were then divided into LTi ($TiO_2 < 3.0$ wt%) and HTi ($TiO_2 > 3.0$ wt%) magma types, following Piccirillo et al. (1988) and Peate et al. (1992). The HTi and LTi samples were further grouped into the several magma types proposed by Peate et al. (1992), following the same chemical classification, and hinging on the La/Yb-Sm/Yb ratios (Pitanga = 9.76–11.56, 2.58–2.86; Urubici = 13.51–16.87, 3.15–4.10; Esmeralda = 2.72–6.35, 1.33–1.59; Gramado = 5.85–10.89, 1.53–2.27). We report in Table 1 the latter geochemical parameters, the topographical references and the magma type for each sample. Our 54 samples range in whole-rock TiO_2 concentration between 0.92 and 4.32 wt% (Fig. 6). Twenty samples classify as HTi magmas and 34 as LTi. The HTi samples are all quite evolved (Mg# = 0.45–0.35; Mg# = atomic Mg/(Mg + Fe^{2+}); Fe_2O_3/FeO = 0.15) and quartz-hyperstene (Q-Hy) CIPW-normative. The LTi samples are similarly Q-Hy CIPW-normative, but show a more variable Mg#, ranging between 0.60 and 0.30.

Considering the 12 samples collected from the FC sequence, eleven are basaltic andesites, all classified as Esmeralda magma type. From QI we collected 10 samples, 2 classified as Esmeralda basalts, and 8 as Pitanga (4 basalts and 4 basaltic andesites). From the BJ1 section we analyzed 6 samples, 2 basaltic andesites of the Gramado magma type, three Urubici basalts and one Urubici basaltic andesite. Finally, from BJ2 we analyzed eighteen Gramado (4 basalts, 11 basaltic andesites, 1 basaltic trachy-andesite and 2 andesites) and eight Urubici samples (7 basalts and 1 andesite).

Pitanga and Esmeralda samples are rather homogenous, and classify mostly as basalts, with the exception of a few basaltic-andesite samples. Among the Urubici magma type the basalts prevail, and the Gramado samples cover the largest range of compositions from basalt to andesite (Figs. 4; 6).

4.2. Petrographic outlines and mineral chemistry

The sampled rocks show an aphyric to slightly porphyritic texture, with a groundmass from glassy (especially from the thinner flows) to

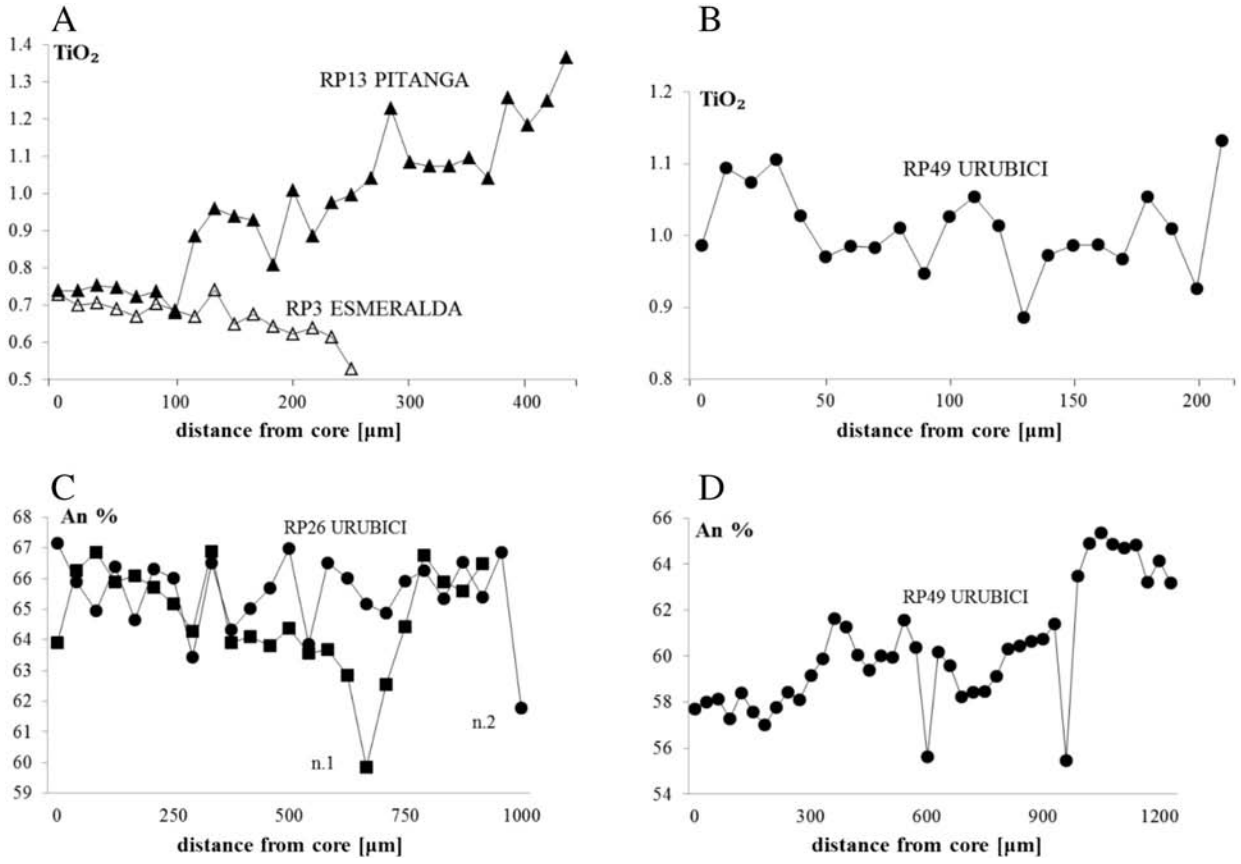

Fig. 5. A: TiO_2 (wt%) variation from the core to the rim in augite crystals of Esmeralda RP3 and Pitanga RP13 samples. B: TiO_2 (wt%) variation from the core to the rim in an augite of Urubici RP49 sample. C and D: Anorthite variation from the core to the rim in plagioclase of sample Urubici RP26 and Urubici RP49, respectively. Distances are in microns.

Table 2

A: microprobe composition of Ca-rich and Ca-poor pyroxenes for the sampled Paraná basalts; Fe^{2+} and Fe^{3+} a.p.f.u. (atoms per formula unit) calculated according to Papike et al. (1974); $Fe^* = Fe^{2+} + Mn + Fe^{3+}$. B: microprobe plagioclase composition of the sampled Paraná basalts. Or = Orthoclase; Ab = Albite; An = Anorthite. C: microprobe composition of magnetite-ilmenite of the sampled Paraná basalts. Mt. = Magnetite; Ilm = Ilmenite. FeO* and Fe_2O_3* calculated according to Carmichael, 1967. Early and Late = early- and late-crystallized phases.

A

	RP1/Esm	RP3/Esm	RP3/Esm	RP8/Esm	RP8/Esm	RP11/Esm	RP11/Esm	RP11/Esm		RP23/Gra	RP27/Gra	RP36/Gra	RP42/Gra	RP42/Gra	RP42/Gra	RP51/Gra	RP51/Gra
	Early	Late	Late	Early	Late	Early	Late	Late		Early	Early	Late	Early	Late	Late	Late	Late
SiO_2 (wt%)	50.33	50.03	51.75	51.91	52.88	49.53	50.32	49.47	SiO_2 (wt%)	53.43	50.66	51.09	51.15	52.56	49.45	51.66	52.24
TiO_2	0.69	0.74	0.30	0.36	0.23	0.55	0.64	0.43	TiO_2	0.20	0.77	0.43	0.62	0.37	0.78	0.34	0.34
Al_2O_3	1.51	1.68	1.01	0.93	0.79	1.18	1.59	0.71	Al_2O_3	0.70	2.02	0.83	1.80	0.75	1.92	3.26	1.88
FeOtotal	16.83	15.51	20.66	22.09	18.90	23.84	18.73	29.36	FeOtotal	16.68	12.18	22.80	14.13	19.93	17.17	5.44	8.25
MnO	0.43	0.34	0.51	0.53	0.39	0.49	0.39	0.62	MnO	0.40	0.31	0.54	0.33	0.42	0.41	0.12	0.26
MgO	13.59	13.02	20.70	19.83	22.03	11.81	13.70	13.08	MgO	24.13	15.30	17.39	16.06	21.66	14.81	17.55	17.66
CaO	16.10	17.80	4.84	4.50	4.28	11.88	14.08	5.48	CaO	4.26	17.52	6.57	14.89	3.95	14.43	20.21	18.35
Na_2O	0.23	0.20	0.06	0.04	0.04	0.16	0.20	0.04	Na_2O	0.02	0.24	0.05	0.17	0.05	0.22	0.14	0.11
Cr_2O_5	0.00	0.00	0.03	0.00	0.04	0.01	0.02	0.01	Cr_2O_5	0.02	0.00	0.01	0.00	0.02	0.02	1.04	0.15
Sum	99.71	99.32	99.86	100.19	99.58	99.45	99.67	99.20	Sum	99.84	99.00	99.71	99.15	99.71	99.21	99.76	99.24
Si	1.9169	1.9115	1.9335	1.9467	1.9648	1.9357	1.9246	1.9560	Si	1.9554	1.9097	1.9466	1.9291	1.9579	1.8838	1.8903	1.9317
Al	0.0678	0.0756	0.0445	0.0411	0.0346	0.0544	0.0717	0.0331	Al	0.0302	0.0897	0.0373	0.0800	0.0329	0.0862	0.1406	0.0819
Fe^{2+}	0.4602	0.4219	0.5704	0.6448	0.5625	0.7249	0.5426	0.9388	Fe^{2+}	0.4612	0.3191	0.6781	0.4067	0.5873	0.4294	0.1264	0.2149
Fe^{3+}	0.0758	0.0737	0.0751	0.0480	0.0247	0.0543	0.0565	0.0321	Fe^{3+}	0.0493	0.0648	0.0483	0.0390	0.0335	0.1176	0.0400	0.0403
Cr	0.0000	0.0000	0.0009	0.0000	0.0012	0.0003	0.0006	0.0003	Cr	0.0006	0.0000	0.0003	0.0000	0.0006	0.0006	0.0301	0.0044
Mg	0.7716	0.7416	1.1530	1.1086	1.2202	0.6881	0.7811	0.7710	Mg	1.3165	0.8598	0.9877	0.9030	1.2028	0.8411	0.9573	0.9735
Mn	0.0139	0.0110	0.0161	0.0168	0.0123	0.0162	0.0126	0.0208	Mn	0.0124	0.0099	0.0174	0.0105	0.0133	0.0132	0.0037	0.0081
Ti	0.0198	0.0213	0.0084	0.0102	0.0064	0.0162	0.0184	0.0128	Ti	0.0055	0.0218	0.0123	0.0176	0.0104	0.0224	0.0014	0.0095
Ca	0.6570	0.7286	0.1937	0.1808	0.1704	0.4974	0.5770	0.2322	Ca	0.1670	0.7076	0.2682	0.6017	0.1576	0.5890	0.7923	0.7270
Na	0.0170	0.0148	0.0043	0.0029	0.0029	0.0121	0.0148	0.0031	Na	0.0014	0.0175	0.0037	0.0124	0.0036	0.0162	0.0099	0.0079
Sum	4.0000	4.0000	3.9999	3.9999	4.0000	3.9996	3.9999	4.0002	Sum	3.9995	3.9999	3.9999	4.0000	3.9999	3.9995	3.9920	3.9992
Ca	33.15	36.79	9.70	9.11	8.60	25.16	29.26	11.74	Ca	8.37	35.94	13.50	30.66	7.94	29.55	41.14	37.03
Mg	38.94	37.44	57.75	55.85	61.60	34.81	39.61	39.00	Mg	65.97	43.67	49.73	46.01	60.60	42.19	49.70	49.58
Fe*	27.05	25.02	32.33	34.90	29.65	39.42	30.38	49.11	Fe*	25.58	19.50	36.58	22.71	31.28	27.44	8.64	12.99

	RP12/Esm	RP17/Pit	RP18/Pit	RP18/Pit	RP18/Pit	RP22/Pit		RP53/Gra	RP53/Gra	RP26/Uru	RP28/Uru	RP28/Uru	RP28/Uru	RP28/Uru	RP28/Uru
	Late	Late	Early	Early	Late	Late		Late	Late	Early	Early	Early	Late	Late	Late
SiO_2 (wt%)	50.92	50.53	50.82	51.47	51.63	49.77	SiO_2 (wt%)	50.27	50.62	49.83	50.87	48.53	49.28	50.13	50.22
TiO_2	0.61	1.22	0.89	1.15	0.96	0.76	TiO_2	0.85	0.33	1.30	0.88	1.76	1.48	0.93	1.03
Al_2O_3	1.81	1.86	1.35	1.53	1.75	1.13	Al_2O_3	1.33	0.82	2.47	1.37	3.15	2.57	1.55	1.72
FeOtotal	13.52	13.20	14.50	11.27	12.73	20.35	FeOtotal	17.27	28.45	16.24	13.90	13.12	13.91	15.89	12.47
MnO	0.36	0.26	0.35	0.27	0.32	0.57	MnO	0.39	0.59	0.38	0.38	0.32	0.35	0.37	0.26
MgO	15.55	14.35	14.59	15.30	15.66	12.25	MgO	12.82	14.75	13.10	13.68	13.03	12.81	14.02	14.95
CaO	16.66	18.04	16.69	18.32	16.16	14.22	CaO	16.30	4.88	16.23	17.96	18.88	18.57	15.96	18.19
Na_2O	0.21	0.22	0.24	0.21	0.22	0.16	Na_2O	0.22	0.11	0.18	0.20	0.29	0.26	0.22	0.26
Cr_2O_5	0.04	0.00	0.00	0.01	0.00	0.00	Cr_2O_5	0.00	0.00	0.09	0.00	0.04	0.05	0.03	0.00
Sum	99.68	99.68	99.43	99.53	99.43	99.21	Sum	99.45	100.55	99.82	99.24	99.12	99.28	99.10	99.10
Si	1.9106	1.9060	1.9248	1.9303	1.9407	1.9327	Si	1.9288	1.9550	1.8972	1.9358	1.8475	1.8793	1.9150	1.8960
Al	0.0800	0.0827	0.0603	0.0676	0.0775	0.0517	Al	0.0601	0.0373	0.1108	0.0614	0.1413	0.1155	0.0698	0.0765
Fe^{2+}	0.3453	0.3641	0.4016	0.3311	0.3972	0.6093	Fe^{2+}	0.5046	0.8767	0.4822	0.4109	0.3342	0.3850	0.4455	0.3017
Fe^{3+}	0.0789	0.0523	0.0576	0.0223	0.0029	0.0516	Fe^{3+}	0.0496	0.0422	0.0349	0.0314	0.0835	0.0586	0.0621	0.0920
Cr	0.0012	0.0000	0.0000	0.0003	0.0000	0.0000	Cr	0.0000	0.0000	0.0027	0.0000	0.0012	0.0015	0.0009	0.0000
Mg	0.8698	0.8069	0.8238	0.8554	0.8775	0.7091	Mg	0.7333	0.8492	0.7435	0.7760	0.7395	0.7283	0.7984	0.8414
Mn	0.0114	0.0083	0.0112	0.0086	0.0102	0.0187	Mn	0.0127	0.0193	0.0123	0.0122	0.0103	0.0113	0.0120	0.0083
Ti	0.0172	0.0346	0.0254	0.0324	0.0271	0.0222	Ti	0.0245	0.0096	0.0372	0.0252	0.0504	0.0425	0.0267	0.0292

(continued on next page)

Table 2 (*continued*)

	RP12/Esm	RP17/Pit	RP18/Pit	RP18/Pit	RP18/Pit	RP22/Pit		RP53/Gra	RP53/Gra	RP26/Uru	RP28/Uru	RP28/Uru	RP28/Uru	RP28/Uru	RP28/Uru
	Late	Late	Early	Early	Late	Late		Late	Late	Early	Early	Early	Late	Late	Late
Ca	0.6697	0.7291	0.6773	0.7361	0.6508	0.5916	Ca	0.6701	0.2019	0.6620	0.7322	0.7701	0.7588	0.6532	0.7358
Na	0.0153	0.0161	0.0176	0.0153	0.0160	0.0120	Na	0.0164	0.0082	0.0133	0.0148	0.0214	0.0192	0.0163	0.0190
Sum	3.9994	4.0001	3.9996	3.9994	3.9999	3.9989	Sum	4.0001	3.9994	3.9961	3.9999	3.9994	4.0000	3.9999	3.9999
Ca	33.84	37.04	34.24	37.55	33.47	29.98	Ca	33.95	10.21	34.20	37.26	39.52	38.91	33.07	36.98
Mg	43.95	40.99	41.65	43.64	45.13	35.93	Mg	37.15	42.93	38.41	39.49	37.95	37.35	40.41	42.28
Fe*	21.44	21.15	23.22	18.03	20.58	33.48	Fe*	28.07	46.45	26.71	22.51	21.44	22.75	25.70	19.79

B

	RP1/Esm	RP1/Esm	RP10/Esm	RP10/Esm	RP11/Esm	RP18/Pit	RP22/Pit	RP23/Gra	RP23/Gra	RP42/Gra	RP51/Gra	RP53/Gra	RP53/Gra
	Late	Late	Late	Late	Early	Late	Early	Early	Late	Late	Early	Late	Late
SiO_2 (wt%)	59.40	56.00	58.28	54.04	58.76	54.17	54.08	52.41	51.45	53.45	49.65	52.33	57.29
TiO_2	0.05	0.05	0.06	0.08	0.09	0.11	0.13	0.06	0.04	0.08	0.02	0.05	0.07
Al_2O_3	24.42	26.56	24.93	27.51	25.42	27.76	27.46	29.05	29.45	27.66	31.13	29.15	25.79
FeOtotal	0.56	0.81	0.65	0.80	0.64	0.74	0.85	0.83	0.82	1.45	0.48	0.70	0.66
CaO	6.76	9.58	7.51	11.10	8.06	10.84	10.82	12.48	13.12	11.04	15.00	12.46	8.44
Na_2O	7.24	5.98	6.99	5.05	7.41	5.09	5.18	4.21	3.92	4.54	2.89	4.31	6.43
K_2O	0.84	0.50	0.74	0.35	0.26	0.44	0.38	0.32	0.28	0.65	0.20	0.27	0.57
Sum	99.27	99.48	99.16	98.93	100.64	99.15	98.90	99.36	99.08	98.87	99.37	99.27	99.25
Or (wt%)	4.79	2.84	4.19	2.03	1.42	2.55	2.19	1.86	1.62	3.86	1.16	1.56	3.27
Ab	62.80	51.54	60.12	68.80	61.57	44.77	45.40	37.20	34.52	41.02	25.55	37.90	56.06
An	32.40	45.63	35.69	29.39	37.01	52.69	52.41	60.94	63.85	55.12	73.29	60.54	40.67

	RP24/Uru	RP24/Uru	RP24/Uru	RP27/Uru	RP27/Uru	RP27/Uru	RP28/Uru	RP28/Uru
	Early	Late	Late	Early	Early	Late	Early	Late
SiO_2 (wt%)	51.52	52.71	51.83	54.33	53.53	57.25	55.07	55.16
TiO_2	0.11	0.14	0.13	0.12	0.07	0.10	0.08	0.07
Al_2O_3	29.55	28.91	29.50	27.35	28.60	26.46	25.71	26.76
FeOtotal	0.71	0.91	0.72	1.34	0.87	0.77	3.28	1.16
CaO	12.92	12.03	13.05	10.71	11.55	8.71	8.97	10.03
Na_2O	3.76	4.40	3.71	5.07	4.51	6.18	5.47	5.34
K_2O	0.31	0.39	0.28	0.31	0.32	0.43	0.32	0.36
Sum	98.88	99.49	99.22	99.23	99.45	99.90	98.90	98.88
Or (wt%)	1.84	2.27	1.66	1.82	1.90	2.51	1.98	2.13
Ab	33.86	38.92	33.41	45.30	40.62	54.81	51.42	48.02
An	64.30	58.81	64.93	52.88	57.48	42.68	46.60	49.85

C

	RP13/Pit	RP13/Pit	RP13/Pit	RP13/Pit	RP13/Pit	RP22/Pit	RP22/Pit	RP22/Pit
	Mt	Ilm	Ilm	Ilm	Ilm	Ilm	Ilm	Ilm
SiO_2 (wt%)	0.06	0.13	0.21	0.04	0.05	0.03	0.02	0.05
TiO_2	20.63	52.59	52.32	51.16	51.04	50.27	50.50	50.00
Al_2O_3	1.76	0.06	0.07	0.00	0.02	0.00	0.06	0.00
FeOtotal	71.51	43.71	43.79	45.71	45.88	46.76	46.42	47.18
MnO	0.41	0.59	0.55	0.55	0.52	0.50	0.56	0.57
MgO	0.62	1.17	1.29	0.89	0.81	1.03	1.03	0.84
CaO	0.03	0.03	0.04	0.00	0.05	0.05	0.09	0.07
Na_2O	0.04	0.00	0.00	0.00	0.00	0.00	0.00	0.00
K_2O	0.00	0.00	0.00	0.02	0.01	0.03	0.00	0.03
Cr_2O_5	0.06	0.02	0.00	0.00	0.00	0.03	0.02	0.00
Sum	95.12	98.30	98.27	98.37	98.38	98.70	98.70	98.74

FeO*	48.48	44.74	44.41	43.93	43.94	42.85	42.93	42.87		
Fe_2O_3*	25.59	−1.15	−0.69	1.98	2.16	4.34	3.87	4.79		
Sum	97.68	98.18	98.20	98.57	98.60	99.13	99.08	99.22		
	RP22/Pit	RP27/Gra	RP27/Gra	RP30/Uru	RP30/Uru	RP30/Uru	RP30/Uru	RP30/Uru		
	Mt	Ilm	Mt	Mt	Ilm	Ilm	Ilm	Ilm		
SiO_2 (wt%)	0.12	0.05	0.24	1.39	0.08	0.05	0.17	0.14		
TiO_2	16.14	49.61	17.38	19.04	48.43	48.66	48.64	49.44		
Al_2O_3	1.54	0.01	1.35	1.42	0.09	0.07	0.05	0.05		
FeOtotal	73.43	47.35	71.89	69.79	47.38	47.30	46.96	45.62		
MnO	0.24	0.55	1.42	1.18	0.45	0.50	0.50	0.64		
MgO	0.21	0.98	0.10	0.51	1.40	1.29	1.44	1.19		
CaO	0.19	0.08	0.02	0.31	0.11	0.11	0.16	0.87		
Na_2O	0.00	0.00	0.02	0.09	0.00	0.00	0.00	0.00		
K_2O	0.00	0.01	0.00	0.11	0.00	0.01	0.01	0.01		
Cr_2O_5	0.08	0.07	0.05	0.04	0.02	0.02	0.07	0.03		
Sum	91.95	98.71	92.47	93.88	97.96	98.01	98.00	97.99		
FeO*	44.20	42.28	44.75	47.33	40.57	40.89	40.68	40.76		
Fe_2O_3*	32.48	5.63	30.17	24.96	7.57	7.13	6.98	5.40		
Sum	95.20	99.27	95.50	96.38	98.72	98.73	98.70	98.53		

intersertal or intergranular. In general, the HTi basalts appear slightly more porphyritic with respect to the LTi.

Plagioclase is always present. It is often euhedral with an evident zoning in crystals larger than 0.5 mm. Pyroxenes are high- and low-Ca clinopyroxenes (augites and pigeonites). Augites are rarely euhedral (mainly in the Gramado and Urubici magma types), and occasionally form a subophytic texture where the groundmass is intergranular or intersertal. The larger crystals of augite appear slightly zoned. Rock samples with a glassy texture show fewer clinopyroxene phenocrysts. Pigeonites, often euhedral, are abundant in the LTi, and scarce in the HTi rocks. Olivine is very rare and present as iddingsitized crystals (mainly in LTi samples) or completely replaced by opaque phases (mainly in HTi basalts). Opaque minerals are quite abundant and often confined to the groundmass. Apatite is occasionally present as accessory mineral, often within plagioclase crystals, rarely in augites and in the groundmass. Secondary phases such as quartz and carbonates are present in small vacuoles, celadonite is confined as blebs in the groundmass. In sample RP27 (Gramado) sillimanite was observed around an isolated crustal xenolith. Rare green amphibole and epidote, probably products of hydrothermal alteration from pyroxene and plagioclase, were found in the most altered samples (LTi).

4.2.1. Pyroxenes

The LTi samples are two-pyroxene (augite and pigeonite) basalts, while pigeonite is very rare or absent in the HTi ones. In general, all the pyroxenes follow the Skaergaard crystallization trend (Nwe, 1975) with the exception of a few Gramado augites showing lower Ca contents. All the early (E = core of the crystals larger than 1 mm grain size) and late (L = microliths or crystal rims) pyroxenes in HTi rocks are augites (QI core: $Wo_{34–37}$; rim: $Wo_{29–37}$; BJ core: $Wo_{34–39}$; rim: $Wo_{33–38}$), while the LTi basalts show both augites (FC core: $Wo_{25–33}$; rim: $Wo_{29–36}$; BJ core: $Wo_{30–35}$; rim: $Wo_{29–41}$) and pigeonites (FC core: Wo_9; rim: $Wo_{8–11}$; BJ core: Wo_8; rim: $Wo_{7–13}$). As observed also by Piccirillo et al. (1988), in some evolved augites (both HTi and LTi), the Si + Al content is higher than 2 a.p.f.u. (atoms per formula unit), suggesting the presence of Al in the octahedral site M1. In general, the Ti content is lower in augite from LTi rocks (0.005–0.025 a.p.f.u.) than from HTi rocks (0.02–0.04 a.p.f.u.). However, augite cores from HTi and from LTi rocks show similar Ti contents (0.020–0.025).

Some Pitanga samples show strongly zoned augite compositions, in particular in terms of Ti contents. This is exemplified in Fig. 5A by the augite from the HTi sample RP13, Pitanga. Its core shows TiO_2 contents (ca. 0.7 wt%) similar to those of augites from the LTi Esmeralda sample RP3. In the middle part of the crystal the TiO_2 content in the Pitanga augite increases to about 0.9–1.0 wt% and reaches even higher values at its rims (about 1.4 wt%). Also some (HTi) Urubici augites appear chemically zoned, but more irregularly (Fig. 5B).

4.2.2. Plagioclase

Plagioclase cores and rims from both HTi and LTi samples have a composition ranging from labradorite to andesine (HTi core: anorthite component $An_{46–64}$; rim: $An_{40–64}$; LTi core: $An_{37–60}$; rim: $An_{35–63}$), the sole exceptions being one bytownite (An_{73}) in the less evolved sample RP51 (Gramado) and two oligoclase ($An_{29–32}$) in the most evolved samples RP10 and RP11 (Esmeralda). Plagioclase crystals are normally zoned with little core-rim variations, with some exceptions observed only within HTi samples. Two analyzed plagioclase crystals from the HTi Urubici basalt RP26 (Fig. 5C), show oscillations in anorthite content (An = 60–67%). The plagioclase crystal from RP49, HTi Urubici basalt (Fig. 5D), shows a general reverse zoning, with An generally increasing from core to rim. Selected mineral compositions are presented in Table 2.

4.3. Rock compositions

4.3.1. Major and trace elements

We compared major and trace element contents of our samples to literature data for Ribeira, Gramado, Esmeralda, Pitanga and Urubici

rocks. In Fig. 6A the several magma types are represented in terms of TiO_2 content (data sources: Piccirillo and Melfi, 1988; Peate et al., 1988; Peate et al., 1992; Peate and Hawkesworth, 1996; Peate, 1997; Peate et al., 1999). The LTi Gramado rocks cover the largest Mg# range, (0.61 to 0.33), consistently with previously analyzed rocks (e.g. Piccirillo et al., 1989). On the contrary, the LTi Esmeralda (Mg# = 0.54–0.30), the HTi Pitanga (Mg# = 0.38–0.35), and the HTi Urubici (Mg# = 0.45–0.38) samples are quite uniform in Mg#. While SiO_2 does not show any correlation with Mg#, Al_2O_3 and CaO are positively correlated with this differentiation index, probably due to plagioclase fractionation. In addition, FeOt is positively correlated with TiO_2 in the LTi samples but not in the HTi ones (Fig. 6B).

As previously shown for the entire P-E LIP (e.g. Bellieni et al., 1984; Piccirillo et al., 1988), HTi rocks are enriched in P, Zr, Nb and light rare earth elements (LREE; Fig. 6C) compared to LTi ones. The difference in other highly incompatible elements such as K_2O and Rb between the two groups is less well defined (Fig. 6D). Moderately incompatible elements like Y and HREE do not show any evident difference among the groups.

LTi samples show a negative correlation between Ni and Zr (Fig. 7A) and a positive one between Rb and Zr (Fig. 7B), while these elements are not correlated in HTi samples. Moreover, Zr correlates positively with elements such as Nb, Ba and REE for all samples, but the correlation slopes are slightly different for LTi and HTi rocks. LTi Esmeralda samples have low and near constant Sr (<200 ppm; Fig. 7E). The HTi Pitanga and Urubici rocks show instead an exponential increase in Sr with Zr. In Urubici samples, Sr increases from 500 to 1100 ppm, with an exponential trend (R^2 = 0.86) that cannot be attributed to differentiation by simple crystal fractionation. LTi Gramado samples are bimodal, some sharing Esmeralda-like low Sr concentrations and others pointing towards the higher Sr contents of HTi samples. Major and trace element compositions are listed in Table 3.

4.3.2. REE and incompatible elements

REE patterns (values normalized to chondritic compositions; Boynton, 1984; Table 4) highlight further differences. LTi samples (Fig. 8A, B) share similar HREE patterns (Dy/Yb_{CN}: Esmeralda = 1.09–1.30; Gramado = 1.16–1.30), but within this group samples of Gramado type are clearly enriched in LREE compared to Esmeralda (La/Sm_{CN} = 2.31–3.24 vs. 1.56–2.58; La/Yb_{CN} = 3.94–7.41 vs. 2.26–4.28, respectively).

In particular, the LTi (both Gramado and Esmeralda) samples show HREE slopes comparable with those of the upper continental crust (UC; Rudnick and Gao, 2003; Dy/Yb_{CN} = 1.27), but at higher concentration. Gramado samples show also the LREE patterns similar to the UC (La/Nd_{CN} = 0.9–1.07 vs. 1.15). Rocks of both Esmeralda and Gramado groups are characterized by negative Eu anomaly (Eu/Eu*: Esmeralda = 0.81–0.88; Gramado = 0.67–0.94; $Eu/Eu^* = Eu_{CN}/((Sm_{CN} + Gd_{CN})/2)$. Notably, among the LTi samples, the least evolved Esmeralda sample RP19 (Mg# = 0.46; Fig. 7A) shows a unique, nearly flat REE pattern (La/Sm_{CN} = 1.28; Dy/Yb_{CN} = 1.21; La/Yb_{CN} = 1.83) and a quite reduced Eu anomaly (Eu/Eu* = 0.94), suggesting either a different source or the absence of crustal contamination (Section 5.2).

The HTi samples (Fig. 8C, D) show enriched REE patterns all characterized by similar LREE enrichment (La/Sm_{CN} average = 2.63 vs. 2.58 for Pitanga and Urubici, respectively) and slightly variable Dy/Yb_{CN} (Dy/Yb_{CN} average = 1.43 vs. 1.74). Their Eu anomaly is negligible (Eu/Eu^*_{CN} average = 0.95 vs. 0.97).

LTi and HTi samples show two different slopes in the Sm/Yb vs. La/Yb plot (Fig. 9A), where all the groups appear distinct. The LTi samples are aligned from a low LREE composition (RP19) towards compositions similar to the UC (Rudnick and Gao, 2003).

The HTi rocks show lower La/Yb_{CN} ratios (4.5 vs. 10: Fig. 8C, D) if compared to the lavas from Tristan da Cunha (Weaver et al., 1987; Weit et al., 2016), but approach more closely the basalts from the Walvis Ridge and Gough island (La/Yb_{CN} = 5.0–7.0 vs. 6.0–7.5; cf. Hoernle et al., 2015). This is particularly true for the Pitanga samples (Fig. 8E).

In the Primitive Mantle-normalized (McDonough and Sun, 1995; Fig. 10A, B) multi-element diagrams, LTi Gramado and Esmeralda samples show negative anomalies in Nb and Ta with respect to K and La, a

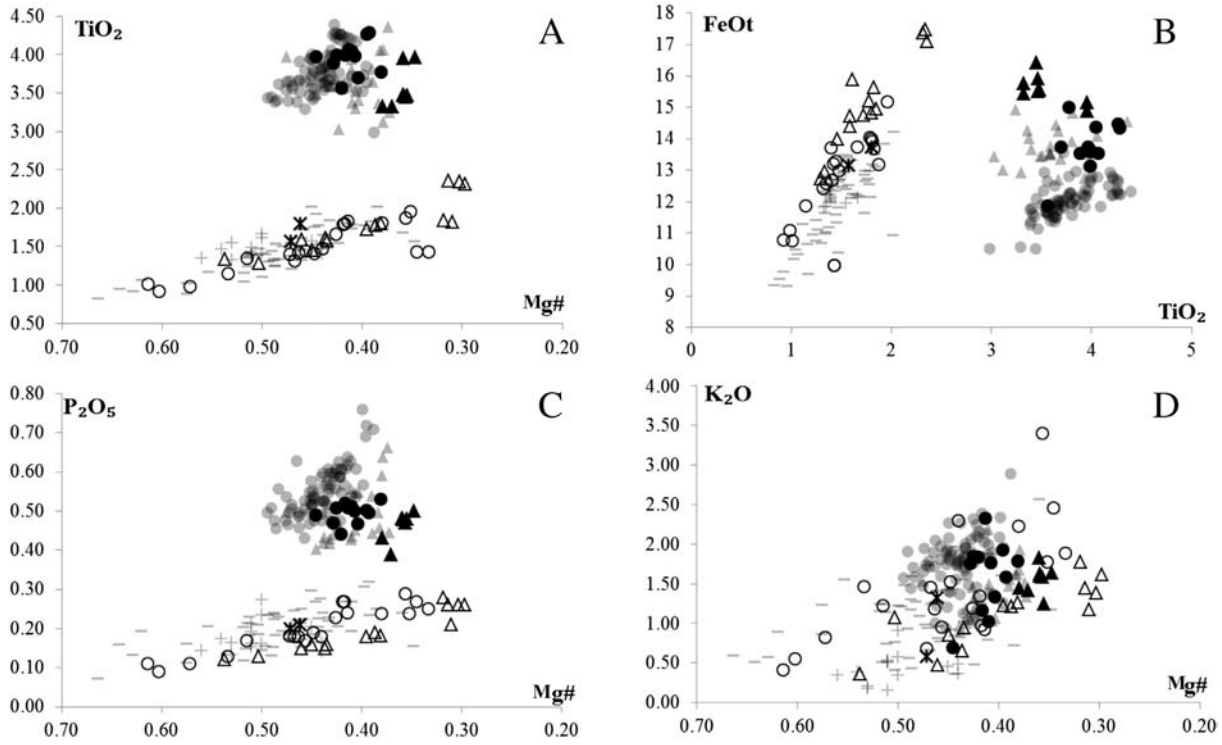

Fig. 6. TiO_2 (A), P_2O_5 (C) and K_2O (D) major elements (wt%) vs. Mg# variations and FeO_{tot} vs. TiO_2 (B) for HTi and LTi basalts. Previously published compositions (crosses = Esmeralda; lines = Gramado; stars = Ribeira; grey full circles = Urubici; grey full triangles = Pitanga) are from Piccirillo and Melfi (1988), Peate et al. (1988; 1992; 1999), Peate and Hawkesworth (1996), Peate (1997), Mg#: atomic $Mg/(Mg + Fe^{2+})$ for Fe_2O_3/FeO = 0.15. LTi: empty triangles = Esmeralda; empty circles = Gramado. HTi = full triangles = Pitanga; full circles = Urubici.

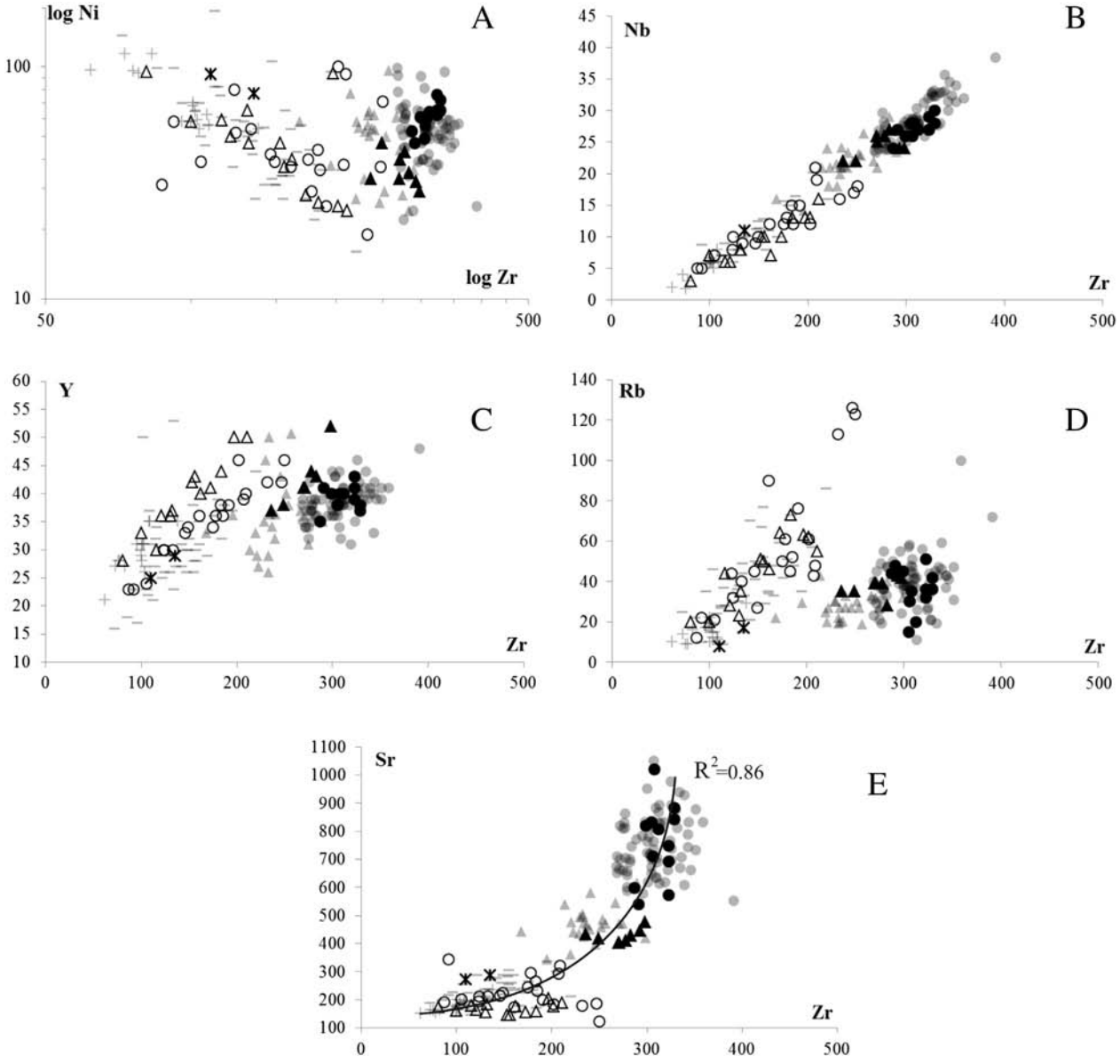

Fig. 7. Trace elements (ppm) vs. Zr (ppm) relationships for HTi and LTi basalt. Data sources and symbols as in Fig. 6. The solid curve in E represents an exponential correlation among all the samples.

positive anomaly in Pb and negative anomalies in Ba, Sr, P, Ti. Globally, these patterns are similar to that of the UC (Rudnick and Gao, 2003), except for Ti and the HREE (including Y). HTi Pitanga and Urubici samples share similar incompatible element patterns, with a positive anomaly in Ba and K (Fig. 10C, D). In Pitanga samples, Sr shows a negative anomaly with respect to Nd, whereas a Sr spike is visible in most Urubici samples. Notably, samples from Tristan da Cunha (Weaver et al., 1987; Weit et al., 2016), the hypothesized present-day hot spot of the Paraná plume, are markedly different in incompatible trace elements with respect to the here studied HTi samples. Tristan rocks mainly show a positive Nb-Ta anomaly, higher Large Ionic Litophile Elements (LILE) values (including K) and a higher La/Yb ratio. Rather, HTi rocks resemble in composition those from the WRG suite (Walvis Ridge-Gough) of Hoernle et al. (2015); Fig. 10E).

4.3.3. Sr-Nd-Pb isotopes

Isotopic compositions of Sr-Nd-Pb were measured in 25 out of 54 samples (Fig. 11). Most of the studied samples have high $^{87}Sr/^{86}Sr_i$ (0.70509–0.71640) and low $^{143}Nd/^{144}Nd_i$ (0.51207–0.51248) initial isotopic compositions (calculated for an age of 134 Ma; Table 4), i.e. positive $\varepsilon_i(Sr)$ varying from 10.62 to 171.14 and negative $\varepsilon_i(Nd)$, from −2.38 to −7.74. Only the LTi Esmeralda sample RP19 has positive ε_i (Nd) (+0.26), coupled with $^{87}Sr/^{86}Sr_i$ of 0.70551. This sample has Sr-Nd isotopic compositions similar to the coeval Jacupiranga carbonatites (Huang et al., 1995). All HTi samples show initial Sr isotopic composition similar to that of sample RP19 (0.70509–0.70606), but lower ε_i (Nd) (from −2.38 to −3.95; $^{143}Nd/^{144}Nd_i$ 0.51248–0.51227), thus plotting between the early Cretaceous carbonatites of Jacupiranga and Anitápolis (Huang et al., 1995; Comin-Chiaramonti et al., 2002). Moreover, the HTi samples have Nd isotopic compositions similar to those of the equivalent rocks of the northern Paraná, coupled with slightly lower $^{87}Sr/^{86}Sr_i$. In comparison, the LTi samples (particularly the Gramado type) show strongly enriched, broadly crustal-like, Sr-Nd isotopic compositions (e.g. $\varepsilon_i(Nd)$ from −3.83 to −7.74; $^{143}Nd/^{144}Nd_i$ 0.51227–0.51207; $^{87}Sr/^{86}Sr_i$ 0.70770–0.71640; Fig. 11A). Notably, the most enriched Gramado samples fall in the field represented by the local Neoproterozoic granites, generated by anatexis of the upper crust during the Brazilian-Pan-African orogeny (Guimarães et al.,

Table 3
Major (wt%), trace (ppm) and incompatible elements (ppm) for the selected LTi and HTi Paraná basalts; Mg# = Mg/(Mg^{+}Fe^{2+}), assuming Fe_2O_3/FeO = 0.15. L.O.I. = loss on ignition; Esm = Esmeralda; Pit = Pitanga; Gra = Gramado; Uru = Urubici. BAS = basalt. TRB = trachy-basalt; BAA = basaltic andesite; BTA = basaltic trachy-andesite; AND = andesite.

	RP1/Esm	RP3/Esm	RP5/Esm	RP6/Esm	RP8/Esm	RP9/Esm	RP10/Esm	RP11/Esm	RP19/Esm	RP20/Esm	RP13/Pit	RP14/Pit	RP15/Pit
	BAA	BAA	BAA	BAA	BAA	BAS	BAA	BAA	BAS	BAS	BAS	BAS	BAS
Lat	25.43° S	25.44°S	25.98°S	25.98°S	25.99°S	25.99°S	26.00°S	26.00°S	26.95°S	26.95°S	26.98°S	26.97°S	26.97°S
Long	51.49°W	51.55°W	51.63°W	51.63°W	51.16°W	51.66°W	51.66°W	51.66°W	52.67°W	52.67°W	52.65°W	52.66°S	52.65°W
SiO_2 (wt%)	53.00	55.17	52.16	52.75	52.07	51.72	52.20	52.21	50.12	50.02	50.03	50.02	50.52
TiO_2	1.72	1.85	1.46	1.79	1.58	1.29	2.35	2.30	1.59	1.60	3.33	3.44	3.47
Al_2O_3	12.96	12.70	13.59	12.84	13.36	14.03	12.12	11.98	13.66	13.22	13.07	12.49	12.77
FeOtotal	14.73	15.00	14.01	14.74	14.36	12.75	17.07	17.27	14.75	15.82	15.47	16.38	15.91
MnO	0.23	0.21	0.21	0.23	0.21	0.20	0.25	0.23	0.22	0.28	0.21	0.21	0.21
MgO	4.59	3.34	5.46	4.33	5.27	6.16	3.72	3.48	6.00	5.84	4.34	4.33	4.18
CaO	8.52	7.12	9.86	8.72	9.25	10.35	7.92	7.21	10.67	9.57	9.36	8.27	8.53
Na_2O	2.64	2.86	2.42	2.59	2.59	2.38	2.44	2.78	2.46	2.48	2.58	2.64	2.73
K_2O	1.22	1.78	0.86	1.26	0.94	1.08	1.44	1.61	0.47	0.65	1.42	1.58	1.25
P_2O_5	0.18	0.28	0.16	0.18	0.16	0.13	0.26	0.26	0.15	0.15	0.39	0.47	0.48
Tot	99.79	100.31	100.19	99.43	99.79	100.09	99.77	99.33	100.09	99.63	100.20	99.83	100.05
mg#	0.39	0.32	0.45	0.38	0.43	0.50	0.31	0.30	0.46	0.44	0.37	0.36	0.36
FeO	12.55	12.71	11.91	12.53	12.21	10.84	14.51	14.68	12.54	13.45	13.15	13.92	13.52
Fe_2O_3	2.43	2.54	2.34	2.46	2.39	2.13	2.85	2.88	2.46	2.64	2.58	2.73	2.65
L.O.I.	0.06	0.04	0.02	0.27	0.06	0.06	0.35	0.06	0.03	0.73	0.55	0.27	0.50
Cr (ppm)	59.70	9.40	42.39	30.70	73.40	84.20	7.70	5.60	50.20	49.40	51.00	36.40	14.13
Ni	45.90	23.10	58.00	36.90	46.50	61.40	25.90	24.80	57.40	49.60	42.40	34.20	35.00
Ba	225.49	309.99	193.00	278.88	216.12	203.57	395.79	389.21	107.09	159.25	497.88	532.82	495.00
Rb	47.31	72.64	17.00	41.16	29.20	37.59	58.49	59.20	14.57	22.07	29.04	33.95	20.50
Sr	155.12	165.44	155.20	186.44	192.09	188.63	220.26	185.33	172.27	170.23	509.87	468.60	420.40
Th	4.46	6.71	3.30	4.22	3.06	3.15	5.21	5.38	1.38	2.59	3.26	3.80	3.30
U	1.21	1.88	0.90	1.07	0.78	0.77	1.23	1.24	0.39	0.73	0.65	0.75	0.60
Pb	6.54	13.12	2.00	24.57	4.78	5.52	7.94	8.13	2.33	4.31	4.14	4.56	1.30
Nb	10.78	15.20	7.10	9.46	7.62	7.36	14.75	15.19	5.95	6.38	24.42	28.37	23.30
Ta	0.73	1.04	0.60	0.59	0.45	0.47	0.93	0.96	0.39	0.43	1.50	1.71	1.50
Zr	153.00	184.00	131.00	162.00	132.00	116.00	197.00	202.00	100.00	121.00	236.00	270.00	283.00
Hf	3.97	4.71	3.00	4.17	3.44	2.99	5.26	5.39	2.68	3.22	5.82	6.79	6.10
Y	39.49	48.95	27.60	44.30	41.63	29.26	58.62	91.13	32.65	40.43	41.22	46.72	31.80

RP16/Pit	RP18/Pit	RP21/Pit	RP22/Pit	RP23/Gra	RP27/Gra	RP31/Gra	RP33/Gra	RP35/Gra	RP36/Gra	RP37/Gra	RP40/Gra	RP42/Gra
BAS	BAS	BAS	BAS	BAA	BAA	BAA	BAS	BTA	AND	BAA	AND	BAA
26.97°S	26.95°S	26.89°S	26.82°S	28.08°S	28.05°S	28.37°S	28.39°S	28.39°S	28.39°S	28.39°S	28.39°S	28.39°S
52.65°W	52.66°W	52.70°W	52.72°W	50.06°W	50.07°W	49.56°W	49.55°W	49.55°W	49.55°W	49.54°W	49.54°W	49.54°W
49.88	51.43	51.19	50.87	52.99	52.60	53.59	51.10	55.43	61.07	53.12	61.13	53.14
3.31	3.95	3.47	3.48	1.15	1.79	1.45	1.39	1.88	1.42	1.67	1.43	1.82
12.88	12.77	12.73	12.68	14.39	13.66	13.91	14.13	13.76	13.80	13.86	13.51	13.52
15.73	14.85	15.55	15.55	11.94	14.07	13.35	13.63	13.23	9.90	13.84	9.98	13.62
0.22	0.18	0.27	0.23	0.19	0.21	0.23	0.20	0.16	0.15	0.21	0.15	0.20
4.59	3.77	4.15	4.15	6.53	4.84	5.35	5.81	3.50	2.36	4.90	2.51	4.59
8.64	8.01	8.14	8.22	9.35	8.52	9.17	9.72	5.63	5.47	9.00	5.79	8.71
2.62	2.74	2.61	2.69	2.35	2.84	2.29	2.59	3.00	3.05	2.61	2.80	2.81
1.44	1.63	1.63	1.60	1.47	1.35	0.96	0.68	3.41	1.87	1.20	2.46	0.92
0.43	0.50	0.48	0.48	0.13	0.27	0.17	0.18	0.29	0.25	0.23	0.27	0.24
99.74	99.83	100.22	99.95	100.49	100.15	100.47	99.43	100.29	99.34	100.64	100.03	99.57
0.38	0.35	0.36	0.36	0.53	0.42	0.46	0.47	0.36	0.33	0.43	0.35	0.41
13.37	12.62	13.22	13.22	10.15	11.96	11.35	11.59	11.25	8.42	11.76	8.48	11.58
2.62	2.48	2.59	2.59	1.99	2.35	2.23	2.27	2.21	1.65	2.31	1.66	2.27
0.14	0.50	0.04	0.12	0.01	0.03	0.51	0.76	2.19	1.48	0.79	1.33	0.48
53.00	5.65	36.30	36.00	81.95	15.50	11.80	24.60	17.20	10.20	32.40	5.65	11.80
42.60	26.00	32.70	34.20	95.00	35.60	39.90	45.90	22.80	15.10	40.80		31.00
502.26	431.00	544.18	564.77	196.00	495.97	234.73	249.71	688.78	578.12	408.92	508.00	346.52
30.39	33.60	34.88	34.10	31.90	39.25	19.81	24.58	115.63	117.98	39.69	130.30	58.37
499.18	449.40	476.54	487.56	185.40	330.82	224.02	220.18	119.92	192.42	259.01	173.30	292.84
3.46	2.90	3.84	3.91	2.70	4.80	4.85	3.71	10.05	11.19	5.04	10.20	5.18
0.69	0.50	0.83	0.78	0.50	0.96	1.20	0.90	2.41	3.30	1.06	2.90	1.35
4.14	0.80	4.28	7.16	2.00	6.44	6.86	5.93	13.35	16.28	6.91	4.40	7.76
26.35	20.50	28.34	27.90	5.40	21.82	11.32	10.69	19.54	21.08	16.26	16.30	16.18
1.63	1.50	1.74	1.67	0.30	1.29	0.69	0.65	1.30	1.52	0.97	1.20	1.06
249.00	298.00	271.00	278.00	123.00	207.00	149.00	124.00	250.00	232.00	183.00	247.00	178.00
6.26	6.60	6.85	6.99	2.20	4.87	3.72	3.20	6.00	6.14	4.34	5.40	4.37
43.58	42.20	46.27	48.95	20.70	42.39	32.67	30.41	49.46	47.22	33.90	31.70	33.80

RP43/Gra	RP46/Gra	RP51/Gra	RP54/Gra	RP24/Uru	RP26/Uru	RP28/Uru	RP29/Uru	RP44/Uru	RP45/Uru	RP47/Uru	RP49/Uru	RP52/Uru
BAA	BAA	BAS	BAA	BAS	BAA	BAS	BAS	BAS	BAS	TRB	BAS	BAA
28.39°S	28.39°S	28.39°S	28.39°S	28.08°S	28.07°S	28.21°S	28.25°S	28.39°S	28.39°S	28.39°S	28.39°S	28.39°S
49.54°W	49.54°W	49.52°W	49.52°W	50.06°W	50.07°W	49.98°W	49.88°W	49.54°W	49.54°W	49.54°W	49.54°W	49.53°W
54.24	53.52	51.50	53.66	51.70	51.68	50.19	50.92	49.39	50.36	50.83	51.72	54.94
1.81	1.96	0.92	1.32	4.00	3.71	3.76	4.32	4.02	3.97	4.07	3.98	3.55
13.48	12.94	14.95	14.32	13.00	13.46	13.18	13.37	13.65	13.40	13.22	13.00	13.41

Table 3 (*continued*)

RP43/Gra	RP46/Gra	RP51/Gra	RP54/Gra	RP24/Uru	RP26/Uru	RP28/Uru	RP29/Uru	RP44/Uru	RP45/Uru	RP47/Uru	RP49/Uru	RP52/Uru
BAA	BAA	BAS	BAA	BAS	BAA	BAS	BAS	BAS	BAS	TRB	BAS	BAA
13.94	15.20	10.77	12.46	13.62	13.80	14.95	14.47	14.28	13.74	13.57	13.66	11.85
0.19	0.22	0.18	0.20	0.17	0.19	0.19	0.18	0.19	0.17	0.17	0.17	0.15
4.08	3.94	7.79	5.22	4.81	4.46	4.39	4.47	4.74	5.27	4.56	4.48	4.10
7.33	7.60	11.02	8.99	8.10	8.67	7.97	8.28	9.24	9.43	8.10	8.18	7.24
2.57	2.79	2.01	2.53	2.49	2.67	2.77	2.80	2.37	2.55	2.79	2.48	2.31
2.23	1.78	0.55	1.46	1.85	1.34	1.78	1.60	1.02	0.69	2.33	1.77	1.83
0.24	0.24	0.09	0.18	0.51	0.47	0.53	0.50	0.51	0.49	0.51	0.50	0.44
100.11	100.19	99.78	100.34	100.25	100.45	99.71	100.91	99.41	100.07	100.15	99.94	99.82
0.38	0.35	0.60	0.47	0.43	0.40	0.38	0.39	0.41	0.45	0.41	0.41	0.42
11.85	12.92	9.15	10.59	11.58	11.73	12.71	12.30	12.14	11.68	11.53	11.61	10.07
2.32	2.53	1.80	2.08	2.27	2.30	2.49	2.41	2.38	2.29	2.26	2.28	1.98
0.40	0.08	0.83	0.02	0.04	0.06	0.02	0.35	1.13	1.66	0.35	0.08	0.50
9.10	11.60	104.56	8.48	59.00	32.10	19.78	42.20	19.78	46.60	54.80	31.90	28.26
23.30	31.70	107.00	38.00	71.80	59.10	45.00	72.50	54.00	61.80	61.90	55.60	57.00
388.80	323.10	179.00	417.00	612.06	610.24	534.00	659.68	576.00	634.10	594.93	638.28	583.00
71.55	56.08	18.80	42.80	27.28	41.60	40.10	31.61	13.40	14.30	45.37	25.23	29.40
198.54	182.10	314.40	216.50	793.35	947.94	501.20	995.97	781.00	927.44	634.16	834.97	602.30
6.61	6.24	2.30	5.10	3.93	4.37	4.30	4.40	4.20	4.53	4.17	4.04	3.80
1.87	1.45	0.30	0.80	0.83	0.98	1.00	1.00	0.90	0.92	0.91	0.87	0.90
9.78	9.09	3.80	3.00	5.60	5.61	0.90	5.99	3.40	6.20	5.93	5.56	1.80
16.44	14.31	4.70	10.80	29.06	30.10	23.40	29.46	23.90	29.40	29.26	28.03	21.90
1.12	0.94	0.20	0.50	1.85	1.98	1.50	1.80	1.60	1.70	1.78	1.54	1.50
191.00	202.00	92.00	175.00	323.00	299.00	291.00	329.00	312.00	305.00	323.00	306.00	287.00
4.62	4.94	2.00	4.20	7.80	7.40	6.30	7.82	7.00	7.74	7.68	7.75	6.60
35.57	48.50	16.70	28.00	46.17	38.02	31.10	36.39	30.70	42.76	38.52	37.71	28.90

2005; Alves et al., 2016). T_{DM}(Nd) depleted mantle model ages calculated following DePaolo (1981a) give different values for the four basalt groups: about 1950 Ma for Esmeralda, 1730 Ma for Gramado, 1350 Ma for Pitanga and 1250 Ma for Urubici. The oldest model age refers to sample RP19 (2640 Ma), which is clearly different from the other Esmeralda samples.

In Pb-Pb isotopic spaces all the here studied Paraná samples cover a wide range of $^{206}Pb/^{204}Pb$ compositions, and all plot above the Northern Hemisphere Reference Line (NHRL; Hart, 1984; Hofmann, 2003; Fig. 11B, C), at compositions typical of enriched mantle reservoirs. We only consider measured values for Pb isotopes, to ease the comparison with previously published data, which are mostly available as measured values only and/or without Pb concentrations, making impossible to calculate the initial isotopic compositions (cf. Cordani et al., 1988; Peate and Hawkesworth, 1996; Peate, 1997; Peate et al., 1999) A clear separation is observed in Pb isotopes between high- and low-Ti magma types, where $^{206}Pb/^{204}Pb = 18.0$ serves as a threshold (Fig. 15B). Samples from the HTi Urubici and Pitanga groups plot at low $^{206}Pb/^{204}Pb$ (17.408–17.753) and samples from the LTi Esmeralda and Gramado groups plot at high $^{206}Pb/^{204}Pb$ (18.052–18.989). The same observation is valid for the $^{207}Pb/^{204}Pb$ ratio, with HTi samples plotting below 15.55 (between 15.508 and 15.545), and LTi samples plotting at distinctly more radiogenic $^{207}Pb/^{204}Pb$ (15.611–15.709). Most of the HTi samples plot on the Geochron line or left of it (Fig. 12). Concerning $^{208}Pb/^{204}Pb$ ratios, the distinction between HTi (low $^{208}Pb/^{204}Pb$; 37.814–38.284) and LTi samples (high $^{208}Pb/^{204}Pb$; 38.312–38.947) is still present, but with a slight overlap at 38.3 (Fig. 11C).

If we exclude the HTi Urubici outlier (sample RP28), the HTi samples cluster more tightly in the Pb-Pb isotopic composition than the LTi samples, which are organized in a more elongated linear trend, extending for a larger range of $^{206}Pb/^{204}Pb$ values (Fig. 11B, C). Furthermore, at comparable $^{206}Pb/^{204}Pb$, Gramado samples plot at slightly higher $^{207}Pb/^{204}Pb$ and $^{208}Pb/^{204}Pb$ values than Esmeralda, and Urubici samples plot at slightly higher $^{207}Pb/^{204}Pb$ and $^{208}Pb/^{204}Pb$ than Pitanga. This characteristic is particularly evident in the $^{208}Pb/^{204}Pb$ vs. $^{206}Pb/^{204}Pb$ space (Fig. 11C). The difference in Pb isotopic compositions between low- and high-Ti basalts is consistent with previously published data (Marques et al., 1999; Peate et al., 1999; Rocha-Júnior et al., 2012, 2013). Neither high- nor low-Ti rocks from the Paraná overlap the isotopic field of the rocks from Tristan da Cunha island and associated seamounts track (Fig. 12; cf. Hoernle et al., 2015). Rather, samples from both Paraná magma types show a good isotopic overlap with rocks from the Gough track, which are isotopically more enriched and show an extreme DUPAL (DUPAL = Dupré-Allègre; Hart, 1984) signature at higher $^{207}Pb/^{204}Pb$ for a given $^{206}Pb/^{204}Pb$).

5. Discussion

5.1. Stratigraphic implications

The here studied sections are largely similar to road profiles and drill cores investigated in previous studies (Peate et al., 1992, 1999; Peate, 1997). In particular, the BJ1 and BJ2 profiles, which are mutually well correlated, show similar alternation of high-Ti Urubici and low-Ti Gramado flows, showing a lava stratigraphy consistent with that described by Peate et al. (1999) for the same area. In particular, the HTi (sampled) flows are less abundant than LTi ones (9 vs. 17). HTi flows are present throughout the sections, but are mostly concentrated in the central portion. No systematic differences were observed in thickness of the lava flows (both groups span from 3 to 50 m thickness) or amount of vacuoles. There are no evident geochemical variations upsection for the Gramado or the Urubici samples. Nevertheless, we note that the most evolved Gramado samples, yielding also the highest $^{87}Sr/^{86}Sr_i$, occur towards the top of the section. In general, and consistently with the observations of Peate et al. (1999), our data support a synchronous emplacement of Urubici and Gramado-type magmas. Peate et al. (1999) sampled an Esmeralda flow on top of the Urubici-Gramado successions at about 100 km north of our sampling sites.

The most significant difference with previous studies concerns the FC and QI road profiles in Santa Catarina State. In the FC section, only Esmeralda rock types are present. The Esmeralda flows immediately below the Chapecó rhyolites are thin (5 m thick), altered and fairly vesicular. Sampled fresh portions appear as rare sub-spherical (max 10–20 cm) masses spread inside the flow. Subsequently, towards the base of the section, the flows grow in thickness (10–15 m) and appear quite fresh. The QI sequence starts and concludes with thin Pitanga

Table 4
Rare earth element (REE) and Sr, Nd and Pb isotopic data for the LTi and HTi Paraná basalts. Esm = Esmeralda, Pit = Pitanga Gra = Gramado; Uru = Urubici. CN = chondrite normalized (Boynton, 1984). Suffixes "m" and "i" = measured and initial (134 Ma) isotopic ratios, respectively.

	RP1/Esm	RP3/Esm	RP5/Esm	RP6/Esm	RP8/Esm	RP9/Esm	RP10/Esm	RP11/Esm	RP19/Esm	RP20/Esm	RP13/Pit	RP14/Pit	RP15/Pit
La	16.58	25.97	12.80	18.20	14.42	12.97	26.19	27.30	8.20	11.35	34.10	39.32	34.90
Ce	40.44	57.89	27.60	44.78	36.28	32.11	59.84	60.28	19.80	28.99	77.56	89.64	72.40
Pr	4.77	6.51	3.95	5.28	4.34	3.80	6.90	7.11	2.78	3.58	8.72	10.05	9.90
Nd	20.45	26.91	16.10	22.52	18.96	16.22	28.09	31.20	13.25	16.22	37.10	42.51	38.20
Sm	5.26	6.33	3.96	5.67	4.98	4.09	7.32	7.87	4.03	4.59	8.02	9.18	7.79
Eu	1.56	1.75	1.19	1.66	1.52	1.27	2.09	2.34	1.39	1.47	2.53	2.81	2.43
Gd	6.20	6.87	4.72	6.41	5.83	4.72	8.36	9.87	5.09	5.62	7.71	8.77	7.71
Tb	1.06	1.16	0.82	1.09	1.00	0.80	1.40	1.60	0.89	0.96	1.16	1.32	1.16
Dy	6.71	7.24	4.82	6.84	6.30	5.01	8.67	9.95	5.64	6.16	6.77	7.67	6.50
Ho	1.43	1.54	1.06	1.44	1.34	1.05	1.82	2.15	1.19	1.31	1.34	1.51	1.24
Er	4.06	4.34	3.06	4.01	3.75	2.96	5.17	6.03	3.34	3.66	3.58	4.08	3.50
Tm			0.44										0.47
Yb	3.81	4.09	2.87	3.71	3.57	2.71	4.72	4.96	3.02	3.38	3.04	3.55	3.02
Lu	0.55	0.60	0.43	0.54	0.53	0.40	0.69	0.73	0.43	0.49	0.43	0.50	0.44
ΣREE	112.88	151.20	83.82	122.15	102.82	88.11	161.26	171.39	69.05	87.78	192.06	220.91	189.66
$(La/Yb)_{CN}$	4.35	6.35	4.46	4.91	4.04	4.79	5.55	5.50	2.72	3.36	11.22	11.08	11.56
$(La/Sm)_{CN}$	3.15	4.10	3.23	3.21	2.90	3.17	3.58	3.47	2.03	2.47	4.25	4.28	4.48
$(Dy/Yb)_{CN}$	1.76	1.77	1.68	1.84	1.76	1.85	1.84	2.01	1.87	1.82	2.23	2.16	2.15
(Eu/Eu^*)	0.83	0.81	0.84	0.84	0.86	0.88	0.81	0.81	0.94	0.88	0.97	0.94	0.95
$(^{87}Sr/^{86}Sr)m$	0.711079		0.709785		0.709040			0.710079	0.705969			0.705942	0.705786
$(^{87}Sr/^{86}Sr)i$	0.709423		0.709190		0.708201			0.708345	0.705510			0.705549	0.705521
$\varepsilon^t(Sr)$	72.09		68.79		54.75			56.79	16.54			17.09	16.70
$(^{143}Nd/^{144}Nd)m$	0.512406		0.512328		0.512403			0.512403	0.512640			0.512391	0.512392
$(^{143}Nd/^{144}Nd)i$	0.512272		0.512200		0.512267			0.512271	0.512482			0.512279	0.512286
$\varepsilon^t(Nd)$	−3.83		−5.24		−3.92			−3.84	0.26			−3.70	−3.56
$(^{206}Pb/^{204}Pb)m$	18.74		18.62		18.20			18.48	18.29			17.63	17.65
$(^{207}Pb/^{204}Pb)m$	15.67		15.66		15.61			15.66	15.61			15.52	15.51
$(^{208}Pb/^{204}Pb)m$	38.77		38.64		38.31			38.64	38.31			37.92	37.99
$(^{206}Pb/^{204}Pb)i$	18.50				17.99			18.28	18.07			17.42	
$(^{207}Pb/^{204}Pb)i$	15.66				15.60			15.65	15.60			15.51	
$(^{208}Pb/^{204}Pb)i$	38.48				38.04			38.36	38.05			37.57	

RP16/Pit	RP18/Pit	RP21/Pit	RP22/Pit	RP23/Gra	RP27/Gra	RP31/Gra	RP33/Gra	RP35/Gra	RP36/Gra	RP37/Gra	RP40/Gra	RP42/Gra
36.21	32.60	39.88	40.83	11.70	30.01	18.99	17.27	37.75	40.60	25.91	33.50	23.28
82.60	68.20	90.14	92.73	23.20	65.20	45.49	41.21	82.59	88.03	56.96	70.70	56.41
9.26	10.60	10.14	10.42	3.50	7.13	5.21	4.72	9.01	9.47	6.32	8.83	6.43
39.12	43.10	42.93	44.10	12.70	29.19	21.59	19.72	36.03	37.23	26.14	32.10	26.61
8.53	9.55	9.26	9.56	3.06	6.53	5.17	4.68	7.84	7.88	5.88	6.92	6.01
2.65	3.06	2.83	2.89	0.96	1.88	1.49	1.46	1.85	1.75	1.70	1.49	1.74
8.10	9.53	8.77	9.05	3.56	6.63	5.55	5.15	7.68	7.62	6.11	6.45	6.21
1.22	1.43	1.32	1.37	0.60	1.07	0.91	0.84	1.23	1.22	0.99	1.04	1.00
7.14	7.89	7.70	7.93	3.57	6.52	5.69	5.28	7.53	7.30	5.99	6.09	6.00
1.42	1.49	1.53	1.58	0.76	1.35	1.17	1.10	1.54	1.50	1.24	1.23	1.22
3.78	3.99	4.05	4.24	2.22	3.78	3.29	3.05	4.34	4.17	3.43	3.40	3.38
	0.54			0.32							0.49	
3.26	3.34	3.52	3.67	2.00	3.50	2.99	2.80	4.07	3.86	3.14	3.05	3.08
0.46	0.51	0.50	0.51	0.31	0.50	0.43	0.40	0.59	0.56	0.45	0.44	0.44
203.75	195.83	222.57	228.88	68.46	163.29	117.97	107.68	202.05	211.19	144.26	175.73	141.81
11.11	9.76	11.33	11.13	5.85	8.57	6.35	6.17	9.28	10.52	8.25	10.98	7.56
4.25	3.41	4.31	4.27	3.82	4.60	3.67	3.69	4.82	5.15	4.41	4.84	3.87
2.19	2.36	2.19	2.16	1.79	1.86	1.90	1.89	1.85	1.89	1.91	2.00	1.95
0.96	0.97	0.95	0.94	0.89	0.87	0.85	0.91	0.72	0.68	0.86	0.67	0.86
	0.706078	0.705953		0.711187	0.708340	0.709086		0.718833	0.719731		0.720061	0.709214
	0.705672	0.705555		0.710253	0.707696	0.708606		0.713593	0.716399		0.715975	0.708132
	18.84	17.18		83.88	47.58	60.49		131.31	171.14		165.12	53.77
	0.512414	0.512387		0.512354	0.512243	0.512348		0.512201	0.512182		0.512191	0.512370
	0.512299	0.512275		0.512228	0.512126	0.512223		0.512088	0.512071		0.512078	0.512252
	−3.30	−3.77		−4.68	−6.67	−4.78		−7.42	−7.74		−7.61	−4.21
	17.75	17.60		18.21	18.05	18.56		18.80	18.98		18.98	18.58
	15.53	15.52		15.63	15.61	15.66		15.69	15.70		15.70	15.66
	38.05	37.85		38.44	38.59	38.68		38.94	38.93		38.93	38.64
		17.36			17.85	18.33		18.56	18.72			18.35
		15.51			15.60	15.65		15.68	15.69			15.65
		37.47			38.28	38.38		38.62	38.63			38.35

RP43/Gra	RP46/Gra	RP51/Gra	RP54/Gra	RP24/Uru	RP26/Uru	RP28/Uru	RP29/Uru	RP44/Uru	RP45/Uru	RP47/Uru	RP49/Uru	RP52/Uru
25.28	26.13	10.00	24.10	43.85	42.68	36.20	44.71	39.40	46.47	42.75	42.70	33.40
60.67	58.90	20.80	51.40	100.14	98.32	78.00	102.35	83.00	104.19	97.97	99.08	72.50
6.80	6.73	2.87	6.24	11.31	11.19	10.63	11.78	10.98	11.82	11.30	11.35	10.02
27.54	28.13	11.20	24.80	49.07	47.86	41.80	50.28	44.60	50.32	48.71	48.79	40.30
6.21	6.68	2.62	5.22	10.96	10.54	8.44	10.86	9.11	10.92	10.86	10.69	8.37
1.66	1.85	0.86	1.41	3.37	3.26	2.66	3.37	2.78	3.39	3.41	3.41	2.65
6.33	7.29	2.97	5.35	10.16	9.55	8.32	9.75	8.37	10.10	9.94	9.79	8.02

Table 4 (*continued*)

RP43/Gra	RP46/Gra	RP51/Gra	RP54/Gra	RP24/Uru	RP26/Uru	RP28/Uru	RP29/Uru	RP44/Uru	RP45/Uru	RP47/Uru	RP49/Uru	RP52/Uru
1.02	1.20	0.51	0.90	1.45	1.37	1.19	1.37	1.24	1.44	1.42	1.40	1.17
6.23	7.45	3.00	5.08	7.96	7.50	6.41	7.39	6.69	7.88	7.83	7.64	6.03
1.28	1.56	0.62	1.04	1.49	1.39	1.19	1.35	1.18	1.47	1.45	1.41	1.09
3.57	4.39	1.78	3.02	3.79	3.49	3.19	3.37	3.02	3.74	3.65	3.56	2.89
		0.24	0.42			0.43		0.41				0.37
3.26	4.01	1.62	2.84	3.08	2.76	2.68	2.65	2.37	2.93	2.86	2.78	2.30
0.47	0.59	0.25	0.40	0.42	0.37	0.38	0.35	0.33	0.40	0.39	0.37	0.32
150.32	154.91	59.34	132.22	247.05	240.28	201.52	249.58	213.48	255.07	242.54	242.97	189.43
7.75	6.52	6.17	8.49	14.24	15.46	13.51	16.87	16.62	15.86	14.95	15.36	14.52
4.07	3.91	3.82	4.62	4.00	4.05	4.29	4.12	4.32	4.26	3.94	3.99	3.99
1.91	1.86	1.85	1.79	2.58	2.72	2.39	2.79	2.82	2.69	2.74	2.75	2.62
0.80	0.81	0.94	0.81	0.96	0.98	0.96	0.98	0.96	0.97	0.99	1.00	0.98
	0.712407	0.708678	0.711850	0.705290	0.705374	0.706499		0.705426		0.705481		0.705864
	0.710734	0.708354	0.710776	0.705103	0.705136	0.706065		0.705333		0.705093		0.705599
	90.72	56.92	91.31	10.76	11.23	24.43		14.03		10.62		17.80
	0.512300	0.512341	0.512214	0.512456	0.512460	0.512441		0.512399		0.512454		0.512374
	0.512176	0.512219	0.512104	0.512339	0.512346	0.512336		0.512292		0.512338		0.512266
	−5.70	−4.86	−7.10	−2.51	−2.38	−2.58		−3.44		−2.54		−3.95
	18.68	18.49	18.48	17.40	17.71	18.33		17.68		17.74		17.54
	15.69	15.66	15.66	15.50	15.54	15.60		15.54		15.53		15.52
	38.90	38.84	38.87	37.81	37.98	38.59		38.22		38.28		38.10
	18.47			17.22	17.56					17.54		
	15.68			15.49	15.53					15.52		
	38.61			37.52	37.76					37.98		

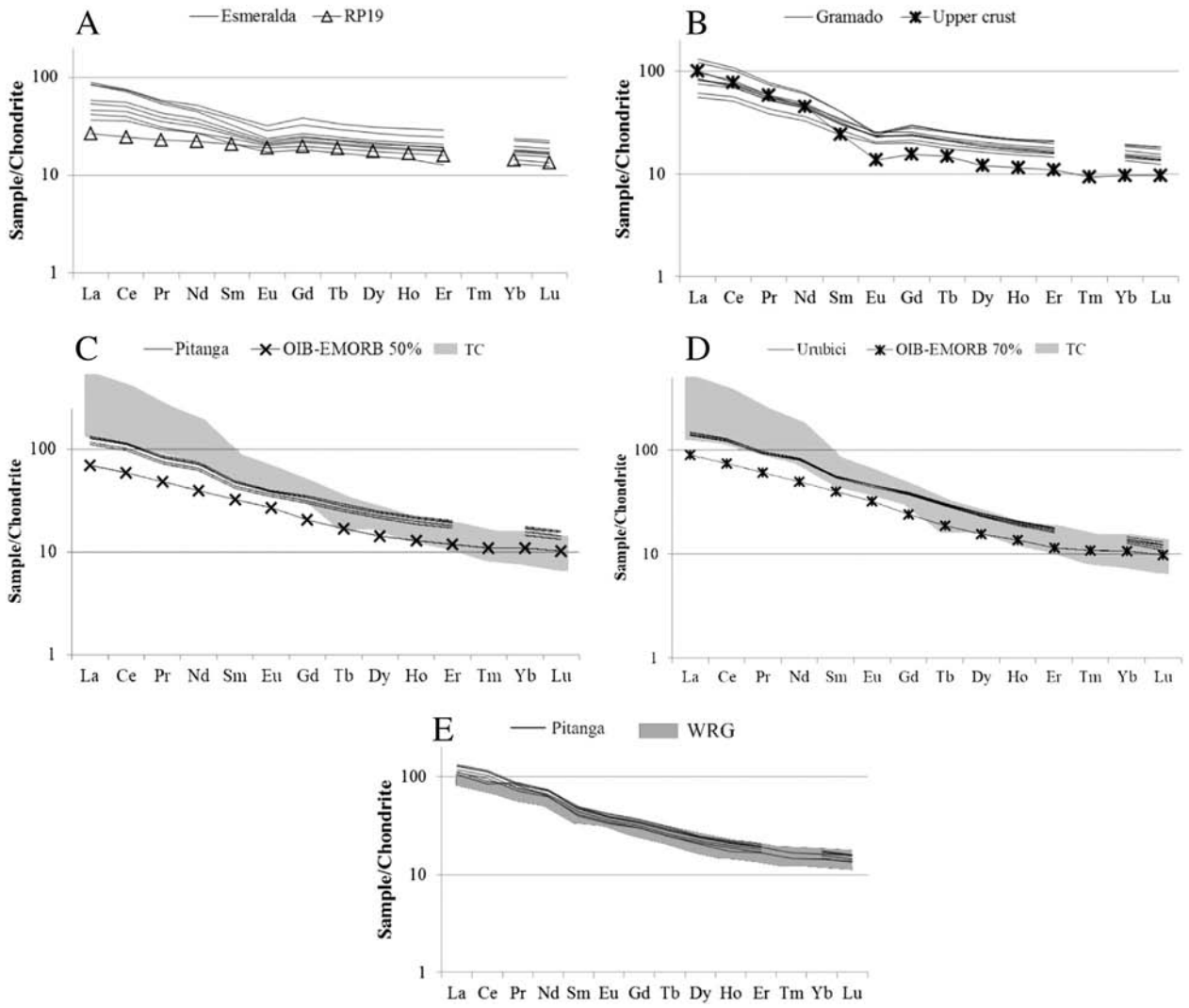

Fig. 8. Rare Earth Elements patterns, normalized to chondrite composition (Boynton, 1984) of the LTi and HTi samples. OIB-EMORB 50% and OIB-EMORB 70% = mixing between OIB and *E*-MORB type (Sun and McDonough, 1989) primary melts. TC = Tristan da Cunha OIB type (Weaver et al., 1987; Weit et al., 2016). WRG = Walvis Ridge-Gough composition (Hoernle et al., 2015). Upper Crust composition from Rudnick and Gao (2003).

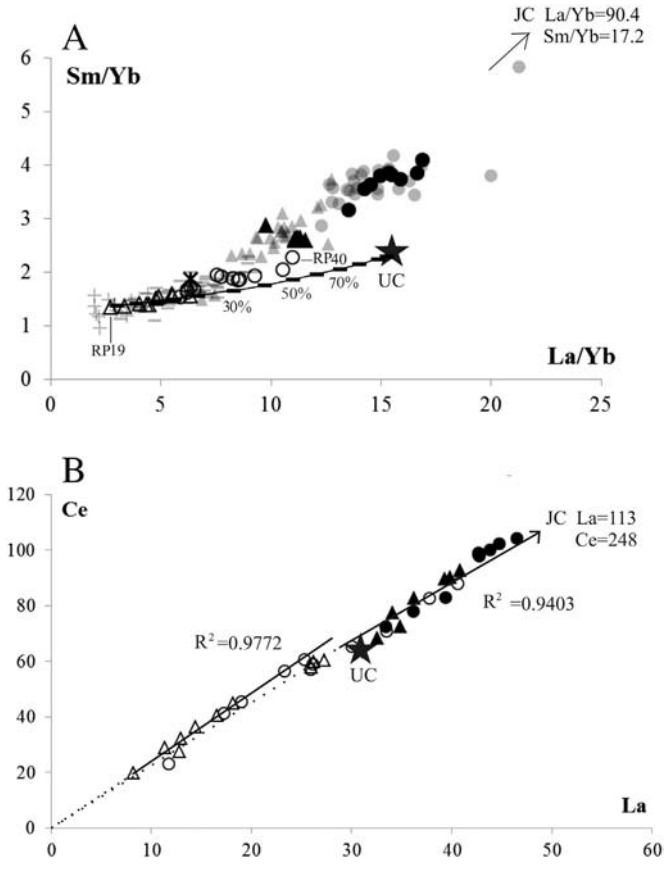

Fig. 9. A: La/Yb vs. Sm/Yb diagram for the LTi and the HTi samples. The dashed line represents a mixing between sample RP19 and the upper crust composition of Rudnick and Gao, 2003; 30-50-70% are the amount of the crust added to RP19. B: La vs. Ce diagram; the bold lines and the dashed one can represent both fractionation and mixing trends. Notably, the Gramado samples gradually move away from Esmeralda trend towards the high-Ti ones. Data sources and symbols as in Fig. 6. Star = UC composition (Rudnick and Gao, 2003); JC = Jacupiranga carbonatite (Huang et al., 1995).

flows. Except for the first flow, which appears altered (though fresh sub-spherical portions could be found), the Pitanga sequence is composed of quite thin and very fresh flow units, sometimes containing small (maximum 3 cm) glassy blebs. The thickness of HTi flows increases near the upper contact with the LTi Esmeralda (about 20 m; Esmeralda LTi RP19 included). The Esmeralda magma type is here present with two consecutive flows with variable thickness (RP19 = 20 m; RP20 = 5 m; Fig. 3A) separated from each other by pahoehoe like structures.

There is no evident up-section variation in geochemistry for the Pitanga samples. In contrast, some variation is observed for the Esmeralda samples. Those collected at lowest height and interlayered with Pitanga flows are relatively Mg-rich and yield the lowest $^{87}Sr/^{86}Sr_i$ and $^{206}Pb/^{204}Pb$ observed within the Esmeralda type. On the contrary, the Esmeralda flows sampled higher in the FC section, right below the Chapecó rhyolites show a progressive up-section depletion in TiO_2 and enrichment in $^{87}Sr/^{86}Sr_i$ and $^{206}Pb/^{204}Pb$. In general, also the volcanostratigraphy from the Santa Catarina state sections (FC and BJ) suggests a contemporaneous emplacement of low-Ti (Esmeralda) and high-Ti (Pitanga) flows, even if the latter are apparently limited to the sampling sites with the lowest elevation.

Based on correlations between drill-core profiles, Peate et al. (1992) suggested a northward migration of the volcanism, with the stratigraphic transition between Esmeralda and Pitanga representing a sort of compositional boundary between sub-provinces – the older, southern, and the younger, northern areas. According to the same authors, the time-related migration of the magmatism and the chemical variations of the southern (Gramado, Urubici, and Esmeralda) vs. the northern (Pitanga, Paranapanema, and Ribeira) magma types can be related to the northward propagation of the rift system during the initiation of continental breakup.

The here presented new stratigraphic and geochemical data show that Esmeralda and Pitanga flows are interlayered about 150 km south of the RS sequence of Peate et al. (1992); Fig. 3). Moreover, chemical zoning of clinopyroxenes show that Pitanga samples yield augites with low-Ti crystal cores (Fig. 5A), compatible with crystallization from a magma with about 2 wt% TiO_2 (for a clinopyroxene/melt partition coefficient of 0.3; cf. Hill et al., 2000). Notably, Esmeralda samples yield TiO_2 in the range 1.3–2.4 wt%, while Pitanga ones have TiO_2 = 3.3–3.9 wt%. This suggests that the clinopyroxene cores of some Pitanga samples crystallized from an Esmeralda magma, providing thus evidence for interaction between Esmeralda and Pitanga magmas in their crustal plumbing systems.

It is interesting to note that the Esmeralda flows from the FC-QI sections (Fig. 13) appear interlayered with Pitanga flows and reach rather high TiO_2 contents (2.30 wt%), almost similar to the HTi basalts. On the contrary, the TiO_2 content is significantly lower (1.30 wt%) in Esmeralda flows from the FC section, which occur at higher elevation and probably at higher stratigraphic levels than those from the QI section. These whole-rock features suggest that early Esmeralda magmas may have interacted with HTi melts.

5.2. Crustal contamination and magma mixing

High- and low-Ti Paraná magmas show markedly different isotopic characteristics. For this reason, and for the strong differences in major and trace element geochemistry observed between the HTi and LTi groups, we exclude that one magma type can be derived from the other by means of closed system evolution (fractional crystallization) or even by partial melting of the same mantle source. Samples of the two magma types are also organized in different trends in most isotopic spaces or trace element vs. isotope plots. For example, in Pb-Pb isotopic spaces LTi rocks are organized in long linear arrays, while HTi rocks show less variable isotopic compositions (Fig. 11). Also, isotopic ratios (i.e. $^{87}Sr/^{86}Sr_i$, $^{206}Pb/^{204}Pb$) are correlated with differentiation indexes (SiO_2 wt% or MgO wt%) for LTi rocks, but not for HTi (e.g. Fig. 15A). Moreover, HTi rocks show trends of enrichment in trace elements (e.g. Sr, Nd, P, Y) that are separated from those of the LTi magmas. This suggests that the different magma types have undergone diverse processes during their evolution, and cannot be related to one another through assimilation.

The isotopic variations observed in the LTi samples along with differentiation indexes suggest an important role of crustal assimilation in the genesis of these rocks. Only the Esmeralda LTi sample RP19 (Figs. 9, 11) seems to have largely escaped crustal contamination, despite its somewhat evolved character (MgO = 6.0 wt%). RP19 shows much higher $^{143}Nd/^{144}Nd_i$ (0.51248) with respect to the samples of the same group. We thus modeled assimilation during fractional crystallization (AFC; DePaolo, 1981b) starting from RP19 as representative of a parental LTi melt.

Critical for a correct modeling of assimilation processes is the choice of reasonable assimilates. The local crust of southern Brazil was largely affected by Brasiliano cycle magmatism. This produced a large amount of acid intrusive rocks (da Silva et al., 2005; Florisbal et al., 2009; Gregory et al., 2015; Alves et al., 2016) and probably left behind a fairly depleted deep crust. We considered Neoproterozoic Garopaba and Paulo Lopes granites (626 Ma; Florisbal et al., 2009) and the Ribeira belt granites (ca. 590 Ma) as possible upper crustal acid contaminants because they mainly crop out close to the Paraná basin (at its easternmost side) and are cut by several Paraná dykes.

In order to calculate potential contribution of older crust, we also considered the granitoids of the Paleoproterozoic (ca. 2.1 Ga) Arroio dos Ratos TTG (Tonalite – Trondhjemite-Granodiorite) suite (Gregory

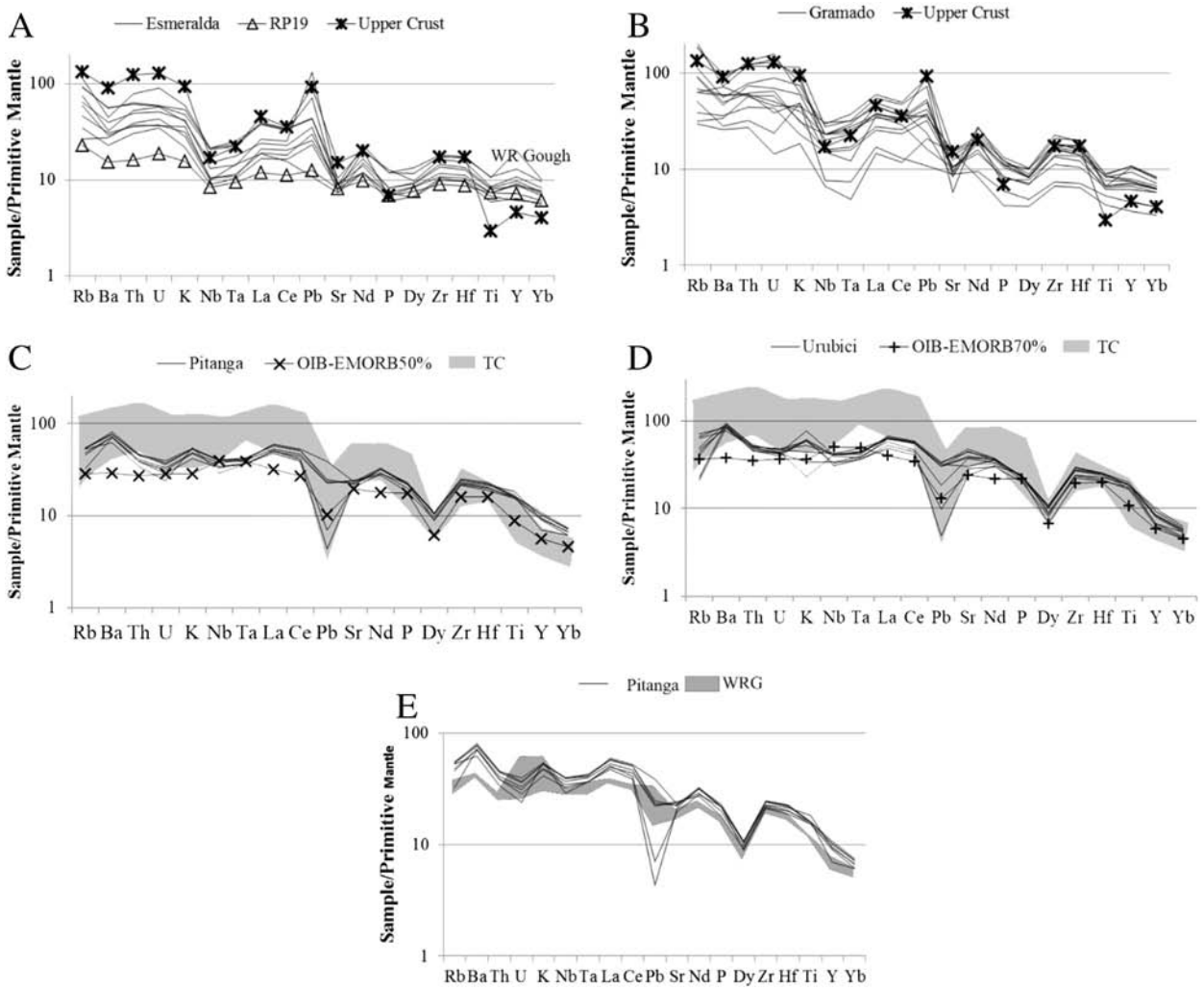

Fig. 10. Multielemental patterns, primitive-mantle-normalized (PM; McDonough and Sun, 1995) plots for LTi and HTi basalts. Data sources and symbols as in Fig. 8.

et al., 2015) as a contaminant candidate. The most evolved LTi samples trend towards high $^{206}Pb/^{204}Pb$ and high $^{207}Pb/^{204}Pb$. These signatures cannot be reproduced by AFC models involving contaminants with relatively low $^{206}Pb/^{204}Pb$ (17–18). This excludes assimilation of the Arroio dos Ratos granitoids and the Ribeira granites, which are relatively depleted in $^{206}Pb/^{204}Pb$. The only crustal reservoirs with high $^{206}Pb/^{204}Pb$ signatures are the Garopaba and Paulo Lopes granites ($^{206}Pb/^{204}Pb$ ca. 19). Using an average composition for these granitoids as upper crustal assimilants, the compositions of most LTi samples are reproduced by significant amounts of assimilation ($r = 0.3$; $F = 0.6$; 6–40%; r = rate of assimilated/fractionated mass; F = residual liquid fraction). This crustal contamination can answer for the isotopic enrichment of all the Esmeralda samples, starting from the composition of Esmeralda sample RP19 (Fig. 14). In contrast, only some of the Gramado samples are reached by the calculated contamination path, whereas the most enriched are out of range, especially in the Sr-Nd isotopic diagram. In summary, crustal contamination of the considered granitoids appears as a key factor in the evolution of all LTi Esmeralda samples and some of the Gramado ones. On the other hand, it is not possible to reconstruct the composition of the most evolved Gramado samples by crustal contamination starting from an Esmeralda parental melt. Some other process must be responsible for the evolution of the Gramado magmas.

Interestingly, for the Esmeralda samples from Santa Catarina State (FC and QI sections), crustal assimilation is more significant for the samples collected at the highest elevation, below the Chapecó rhyolites, while the flow RP19, interlayered between Pitanga flows, is uncontaminated (or less contaminated). Similarly, in the BJ sections the most evolved and most contaminated Gramado samples were collected towards the top of the lava pile. In general, this suggests a time-related increase of crustal contamination for Low-Ti magmas.

Unlike LTi magmas, HTi ones show a rather restricted range in trace element and isotopic compositions. This hinders modeling of AFC processes. Our data do not show any evidence of isotopic variations correlated with differentiation indexes or any compositional trend towards the local crustal rocks. These features do not support any significant role of crustal assimilation. Consistently, the Os isotopic composition of some HTi Paraná rocks is typical of mantle-derived magmas that did not assimilate significant amounts of crustal rocks (Rocha-Júnior et al., 2012). Therefore, interlayered and thus synchronous lava flows show markedly different behavior in terms of crustal contamination, i.e. HTi magmas are virtually uncontaminated while most LTi samples are contaminated.

The genesis of HTi samples appears influenced by other processes, such as magma mixing. In particular, strong zoning in TiO_2 contents observed in augites from Pitanga samples (and, to a lesser extent, in Urubici) suggests interactions between high and low-Ti magmas in the magma plumbing system before emplacement of these flows. Also, some Gramado samples show enrichments in Sr concentration at decreasing $^{87}Sr/^{86}Sr_i$ (Fig. 15B), i.e. they trend towards Urubici or HTi compositions, in general. We argue that this might be a further reflection of magma mixing occurring between high- and low-Ti magma types, as also supported by the alternation between Urubici and Gramado flows observed by Peate et al. (1999).

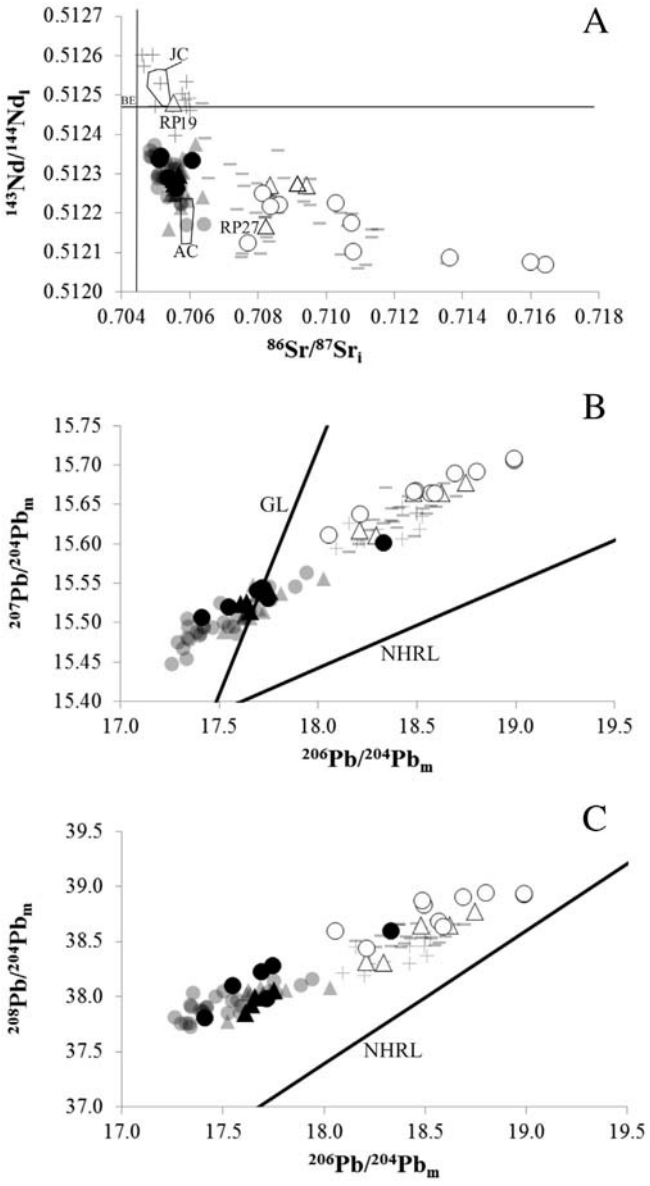

Fig. 11. Isotopic ratios (A: $^{87}Sr/^{86}Sr_i$ vs. $^{143}Nd/^{144}Nd_i$; B: $^{207}Pb/^{204}Pb_m$ vs. $^{206}Pb/^{204}Pb_m$; C: $^{208}Pb/^{204}Pb_m$ vs. $^{206}Pb/^{204}Pb_m$) of the studied HTi and LTi basalts. Symbols and data sources for Paraná basalts as in Fig. 6. AC = Anitápolis carbonatites (Comin-Chiaramonti et al., 2002); JC = Jacupiranga carbonatites (Huang et al., 1995); BE = Bulk Earth values were recalculated for an age of 134 Ma and are $^{87}Sr/^{86}Sr_i = 0.70434$ and $^{143}Nd/^{144}Nd_i = 0.51247$; NHRL = North Hemisphere Reference Line; GL = Geochron Line.

5.3. Lithospheric mantle contribution

A prominent role of the SCLM in the genesis of the Paraná magmas has been suggested by several authors (e.g. Piccirillo et al., 1988; Gibson et al., 1995; Rosset et al., 2007; Rocha-Júnior et al., 2012, 2013; Comin-Chiaramonti et al., 2014). Although extensive wholesale melting of the lithospheric mantle seems hard to conceive, it should be considered that Paraná magmatism took place over a mobile belt system (Peate, 1997) where the SCLM can be enriched by subducted material. The coeval alkaline and carbonatitic complexes that surround the Paraná basin further suggest that the shallow mantle was fluxed by large amounts of water and CO_2. Geophysical evidence for enriched lithospheric roots beneath the Paraná basin has been recently put forward by Chaves et al. (2016). These authors suggest that the high P-wave velocity in the mantle below the Paraná reflects an increase of the lithospheric density, suggesting a metasomatic refertilization of the Paraná

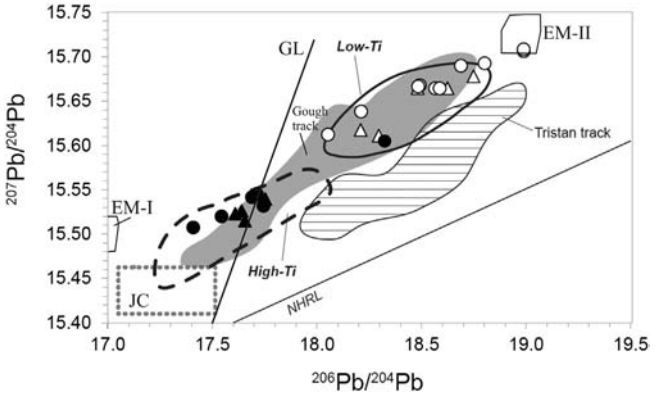

Fig. 12. $^{207}Pb/^{204}Pb_m$ vs. $^{206}Pb/^{204}Pb_m$ diagram for the sampled Paraná basalts. NHRL = North Hemisphere Reference Line; GL = Geochron Line. HTi and LTi fields data sources and symbols as in Fig. 6. JC = Jacupiranga carbonatites (Huang et al., 1995); Gough and Tristan Walvis Ridge tracks from Hoernle et al. (2015). EM-I and EM-II values are from Zindler and Hart (1986).

lithosphere. The metasomatic agents may be represented by asthenospheric components formed within the mantle wedge during the Proterozoic subduction event. The generation of the voluminous Paraná basalts is possibly related to this metasomatic event.

Interaction between the peridotitic mantle source of the Paraná basalts and a carbonatitic component is suggested by the strong enrichment in elements such as Sr, P or Ta in Paraná basalts (Urubici in particular). These elements are particularly concentrated in carbonatites, which are abundant in the Paraná basin. In a Sr vs. $^{87}Sr/^{86}Sr_i$ plot, HTi samples align in a clear trend of rapidly increasing Sr concentration (from 420 to 947 ppm) at constant $^{87}Sr/^{86}Sr_i$. In particular, the samples plotting at higher Sr concentrations are those from the Urubici group. This can also be observed in other trace element (e.g. Nd, P, Nb, Zr) vs. isotope ($^{87}Sr/^{86}Sr_i$; $^{206}Pb/^{204}Pb$; $^{207}Pb/^{204}Pb$) plots. This behavior suggests hybridization of the parental HTi melts, via simple magma mixing, with an end-member very rich in trace elements (mostly Sr, P, Zr, Nb, Ta) and with Sr isotopic signature similar to that of the HTi Paraná magmas, i.e. $^{87}Sr/^{86}Sr_i$ around 0.705. This end member can plausibly be recognized in the Jacupiranga carbonatites (Fig. 16; Huang et al., 1995). It is also interesting to note that the Urubici samples reach slightly higher Nb/Ta ratios compared to Pitanga samples (15–19 vs. 15–17). Combined with a lack of Ti anomalies, this seems compatible with a contribution from a titanite-bearing carbonatite source (John et al., 2011). In general, the trace element enrichment is not correlated with isotopic compositions, thus it is unlikely to be produced by crustal assimilation, and suggests instead an enrichment of the source. The isotopic homogeneity of both Pitanga and Urubici HTi rocks and their similarity with local carbonatites (e.g. Jacupiranga) supports furthermore that the enrichment process imparting the carbonatitic signature was relatively recent.

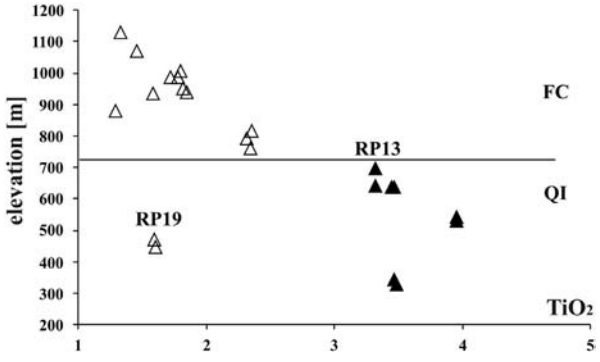

Fig. 13. TiO_2 vs. elevation (m) of the FC and QI sections. Symbols as in Fig. 6.

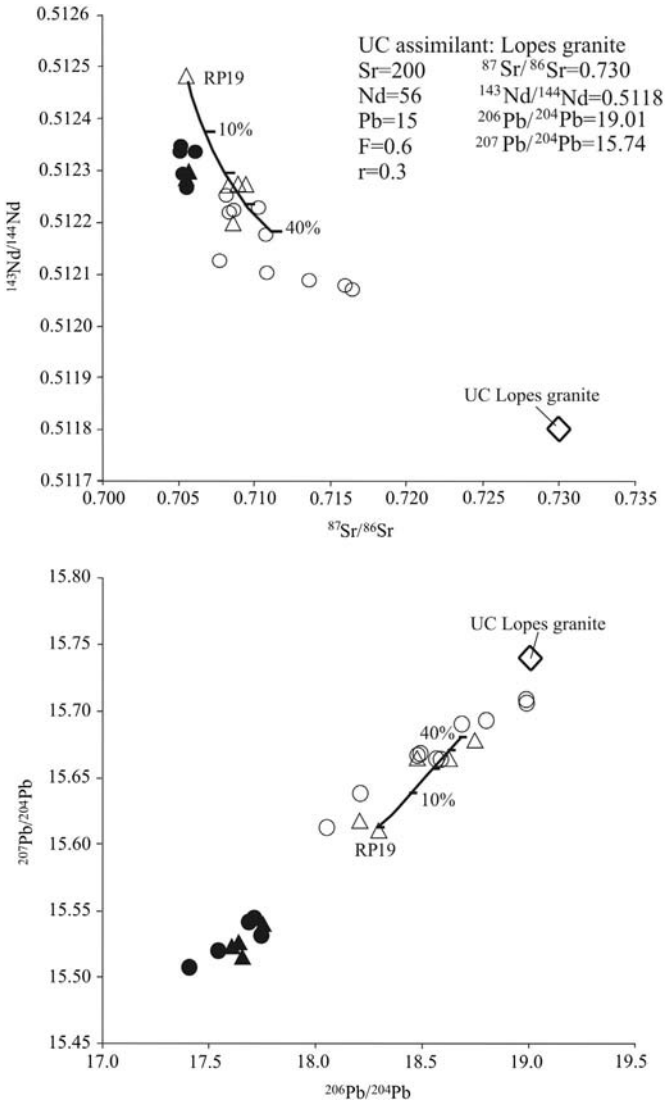

Fig. 14. A: $^{87}Sr/^{86}Sr_i$ vs. $^{143}Nd/^{144}Nd_i$ and B: $^{207}Pb/^{204}Pb_m$ vs. $^{206}Pb/^{204}Pb_m$ for the Paraná basalts; symbols as in Fig. 6. Dashed line = AFC between Esmeralda RP19 and the Upper Crust represented by the Lopes granites (Florisbal et al., 2009); 10–40% = amount of crustal assimilation.

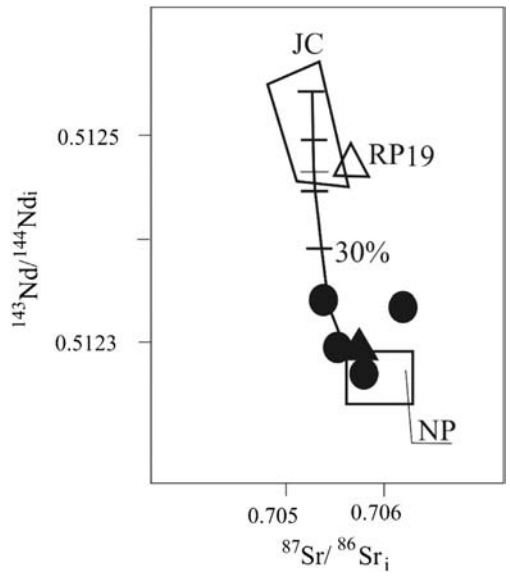

Fig. 16. $^{87}Sr/^{86}Sr_i$ vs. $^{143}Nd/^{144}Nd_i$ for the studied HTi basalts; solid line represents the mixing between the North Paraná (NP; Paranapanema) HTi (Piccirillo et al., 1988; Rocha-Júnior et al., 2013) and the Jacupiranga carbonatites (Huang et al., 1995). Tick mark of 30% represents the higher amount of Jacupiranga carbonatites in the HTi basalts. Symbols as in Fig. 6.

The introduction of a carbonatitic component is most likely to have occurred as an SCLM contribution to melts rising from below the lithosphere. Rocha-Júnior et al. (2013) support an arc mantle peridotite as the main asthenospheric mantle source for the Paraná magmatism, and our data show no contradiction to this model. The experiments of Burov and Cloetingh (2009) suggest that a plume impinging against an old stratified lithosphere, proceeding towards the surface can provoke a subduction-like down thrusting of the mantle lithosphere to 400 km depth. Such a collapse of the lithosphere leads to the breakdown of water- and CO_2-rich phases. The presence of volatiles can significantly lower the peridotite solidus, in particular at the lithospheric-asthenospheric boundary (Wyllie, 1989; Hirose, 1997; Hirschmann, 2000; Till et al., 2010; Dasgupta et al., 2013). This may create low volume melts that, percolating as porous flows through the peridotite matrix, fractionate chromatographically (Navon and Stolper, 1987), with the more incompatible elements migrate up within the lithospheric mantle. Mattielli et al. (1999), studying the evolution of a heterogeneous lithospheric mantle in a plume environment, identified this kind of metasomatism in lithospheric mantle xenoliths and argued that these metasomatic effects occurred relatively shortly before the eruptive event. Finally, Tappe et al. (2006) indicate that the lithosphere-asthenosphere boundary can be roughly considered as a transition between the porous and the channelized flow regime. Carbonatite-phlogopite dominated veins are expected to form in the lithosphere because CO_2-bearing melts are forced to crystallize in contact with the

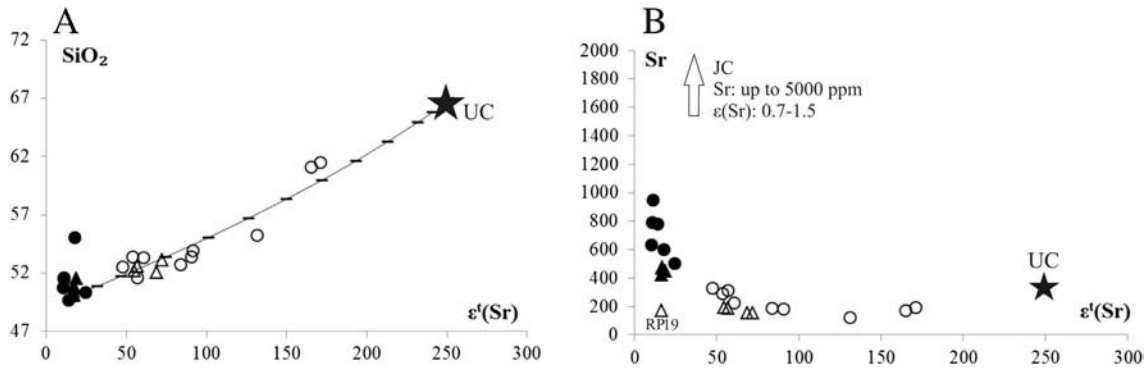

Fig. 15. A: $\varepsilon_i(Sr)$ vs. SiO_2 diagram for the HTi and LTi basalts. The dashed line represents the mixing line between $\varepsilon_i(Sr)$ and the SiO_2. B: $\varepsilon_i(Sr)$ vs. Sr. Data sources and symbols as in Fig. 6 and Fig. 9. UC isotopic composition is from Harmon et al. (1984), Jacupiranga carbonatite values (JC) from Huang et al., 1995.

lithosphere, given their low heat capacity. These veins can easily re-melt during subsequent lithospheric thinning.

5.4. Mantle plume contribution

All Paraná samples, including those apparently not affected by crustal or carbonatitic contamination, yield a strongly enriched isotopic signature. This enriched signature can be due to enrichment processes, principally recycling of old subducted material affecting the shallow (Rocha-Júnior et al., 2012, 2013) or the deep mantle (e.g. Ewart et al., 2004; Hoernle et al., 2015). In particular, a contribution of the Tristan da Cunha or Gough mantle plumes has been suggested (e.g. Ewart et al., 2004; Hoernle et al., 2015). The latter authors in particular analyzed seamount samples from the Walvis Ridge, which overlap the Gough track, yielding strongly enriched signatures plotting between EM-I and EM-II end members (Fig. 12). Among the here presented data, a possible contribution of Gough-type mantle can be traced in Pitanga samples. These overlap in trace element and Pb isotopic composition with some of the most EM-I-like samples from the Walvis Ridge reported by Hoernle et al. (2015). While Hoernle et al. (2015) attribute the marked EM-I (or DUPAL) signature to a deep mantle origin, other authors (e.g., Peate et al., 1999; Iacumin et al., 2003; Rocha-Júnior et al., 2013) attribute its origin to enriched portions of the SCLM.

Although plume models for the genesis of the Paraná CFBs are alive, they do not lack pitfalls. These may reside in the immobility of the African plate since Cretaceous times and in the mismatching position of the Tristan plume, located some 1000 km away from the Paraná basin in the lower Cretaceous as demonstrated through paleomagnetism (Ernesto et al., 2002). A deep asthenospheric origin for the Paraná is also discarded by the fact that basalts of different ages from similar cratonic domains in South America show similar chemical patterns which are suggestive of a chemical imprinting of the past cratonization (Iacumin et al., 2003).

6. Conclusions

A detailed combined stratigraphic and geochemical study of four new lava sequences was carried out aiming at furthering our understanding of the Paraná magmatism. Chemical classification of the magma types allowed to recognize an overall consistency between the new sections and the lava piles described in the literature (e.g., Peate et al., 1992, 1999). New recognized features are the interlayering of Esmeralda and Pitanga flows, never observed before, and the evidence for interactions between high- and low-Ti magmas, inferred from variations in TiO_2 contents in augites from Pitanga flows. Isotopically, the newly sampled Esmeralda and Gramado basalts and basaltic andesites cover the isotopic fields previously observed for low-Ti Paraná rocks, and the same happens for high-Ti Pitanga and Urubici flows. Two different sources and petrogenetic processes are inferred for the two magma groups. In particular, low-Ti magma types show higher radiogenic $^{206}Pb/^{204}Pb$ and $^{87}Sr/^{86}Sr_i$, which are correlated with differentiation indexes. This suggests that low-Ti magmas (the most evolved Esmeralda and a few Gramado samples) experienced assimilation processes during fractional crystallization and were chiefly contaminated by moderate amounts (5–30%) of acid upper crustal rocks, potentially identified in the Paulo Lopes granites and the Garopaba granitoids suites (Florisbal et al., 2009). Upper crustal assimilation is also supported by the presence of sillimanite crystals around a crustal xenolith found in a Gramado flow. Crustal contamination gets stronger proceeding up-section in Esmeralda samples, revealing a time-related intensification of this process. High-Ti magma types appear to have largely escaped crustal contamination, but their enrichment in trace elements (e.g., P, Sr) at relatively constant isotopic signatures seems to reflect a mixing process between a parental mantle melt and a carbonatitic source similar to that of Jacupiranga carbonatites (Huang et al., 1995), encountered in the lithospheric mantle. A general picture arises of a very complex origin for the Paraná magmatism, where different sources and processes (carbonatite-tholeiitic magma mixing in the source and assimilation of acid upper crust en-route to the surface) are responsible for the genesis of the high- and low-Ti magmas, respectively. The lack of compositional continuity (e.g., in Pb vs. Pb isotopic spaces) and the clear separation in different trends in trace element vs. trace element variation diagrams support in general a scarce interaction between high- and low-Ti magma types. The only exceptions are represented by Pitanga-Esmeralda mixing inferred by pyroxene crystal chemistry, and by Gramado and Urubici mixing, visible by the increase in Sr and trending towards high-Ti geochemical fields observed in some Gramado samples. Separation between high- and low-Ti magma chambers seems therefore likely, with only occasional interactions occurring along the plumbing systems. Low Pb isotopic composition for high-Ti Paraná rocks overlap well with the Gough island track magmas and do not share the generally more depleted signatures of Tristan da Cunha track rocks (cf. Hoernle et al., 2015). This argues against derivation of the Paraná magmatism from the Tristan hot spot, as previously suggested, but highlights the presence of a strong DUPAL signature for these CFBs. Strongly debated is the origin of the DUPAL signature and the Paraná-Etendeka LIP, be it from a mantle plume system or from merely lithospheric sources. A common, recent tendency is that of tracking the source of the Paraná-Etendeka magmatism down to the core-mantle boundary through the LLSVP (Large Low Shear Velocity Province; Burke et al., 2008; Steinberger and Torsvik, 2012) margins, due to spatial association between these margins and the original (at 134 Ma) position of the Paraná-Etendeka eruptive center (Hoernle et al., 2015). It is highly speculative and beyond the scope of this contribution to discern between deep or shallow mantle provenance of the (DUPAL flavored) Paraná magmatism, but we stress that a strong lithospheric imprinting is visible in our and previously studied volcanics from the Paraná.

Acknowledgement

This contribution is in memory of our colleague and friend Enzo M. Piccirillo. We thank L. Furlan (thin sections), R. Carampin (EMP analyses), C. Bassoulet and M Rouget (ICP.MS). The Italian National fund PRIN 2008 (Protocol 2008CR4455_003) and the São Paulo Research Foundation (FAPESP; process n. 11/10508-6) supported this research. Detailed reviews by two anonymous reviewers helped us to improve the original version of this work.

Appendix A. Supplementary data

Supplementary data to this article can be found online at http://dx.doi.org/10.1016/j.jvolgeores.2017.08.009.

References

Alves, A., Janasi, V.A., da Costa Campos Neto, M., 2016. Sources of granite magmatism in the Embu Terrane (Ribeira Belt, Brazil): Neoproterozoic crust recycling constrained by elemental and isotope (Sr-Nd-Pb) geochemistry. J. S. Am. Earth Sci. 68, 205–223.

Anderson, D.L., 1994. The sublithospheric mantle as the source of continental flood basalts; the case against the continental lithosphere and plume head reservoirs. Earth Planet. Sci. Lett. 123, 269–280.

Baker, J., Peate, D., Waight, T., Meyzen, C., 2004. Pb isotopic analysis of standards and samples using a ^{207}Pb-^{204}Pb double spike and thallium to correct for mass bias with a double-focusing MC-ICPMS. Chem. Geol. 211, 275–303.

Barrat, J.A., Keller, F., Amossé, J., Taylor, R.N., Nesbitt, R.W., Hirata, T., 1996. Determination of rare earth elements in sixteen silicate reference samples by ICP-MS using a Tm addition and an ion exchange chromatography procedure. Geostand. Newslett. 20, 133–139.

Beguelin, P., Chiaradia, M., Beate, B., Spikings, R.A., 2015. The Yanaurcu volcano (Western Cordillera, Ecuador): a field, petrographic, geochemical, isotopic and geochronological study. Lithos 218-219, 37–53.

Bellieni, G., Comin-Chiaramonti, P., Marques, L.S., Melfi, A.J., Piccirillo, E.M., Nardy, A.J.R., Roisenberg, A., 1984. High- and low-TiO_2 flood basalts from the Paraná plateau (Brazil): petrology and geochemical aspects bearing on their mantle origin. Neues Jahrbuch Miner. Abh. 150 (3), 273–306.

Boynton, W.V., 1984. Cosmochemistry of the rare Earth elements: meteorite studies. In: Henderson, P. (Ed.), Rare Earth Element Geochemistry. Elsevier, Amsterdam, pp. 63–114.

Bryan, S.E., Ernst, R.E., 2008. Revised definition of Large Igneous Provinces (LIPs). Earth Sci. Rev. 86, 175–202.

Burke, K., Steinberger, B., Torsvik, T.H., Smethurst, M.A., 2008. Plume generation zones at the margins of large low Shear velocity provinces on the core-mantle boundary. Earth Planet. Sci. Lett. 265, 49–60.

Burov, E., Cloetingh, S., 2009. Controls of mantle plumes and lithospheric folding on modes of intraplate continental tectonics: differences and similarities. Geophys. J. Int. 178, 1691–1722.

Callegaro, S., Marzoli, A., Bertrand, H., Chiaradia, M., Reisberg, L., Meyzen, C., Bellieni, G., Weems, R.E., Merle, R., 2013. Upper and lower crust recycling in the source of CAMP basaltic dykes from southeastern North America. Earth Planet. Sci. Lett. 376, 186–199.

Carmichael, I.S.E., 1967. The iron titanium oxides of salic volcanic rocks and their associated ferromagnesian silicates. Contrib. Mineral. Petrol. 14, 36–64.

Chaves, C., Ussami, N., Ritsema, J., 2016. Density and P-wave velocity structure beneath the Paraná Magmatic Province: refertilization of an ancient lithospheric mantle. Geochem. Geophys. Geosyst. 17 (8), 3054–3074.

Chiaradia, M., Müntener, O., Beate, B., 2011. Enriched basaltic andesites from mid-crustal fractional crystallization, recharge, and assimilation (Pilavo Volcano, Western Cordillera of Ecuador). J. Petrol. 52 (6), 1107–1141.

Coltice, N., Phillips, B.R., Bertrand, H., Ricard, Y., Rey, P., 2007. Global warming of the mantle at the origin of flood basalts over supercontinents. Geology 35 (5), 391–394.

Comin-Chiaramonti, P., Gomes, C.B., 2005. Mesozoic to Cenozoic Alkaline Magmatism in the Brazilian Platform. Edusp (Editotra da Universidade de São Paulo)/Fapesp (Fundação de Amparo à Pesquisa do Estado de São Paulo). São Paulo.

Comin-Chiaramonti, P., Bellieni, G., Piccirillo, E.M., Melfi, A.J., 1988. Classification and petrography of continental stratoid volcanics and related intrusives from the Paraná basin (Brazil). In: Piccirillo, E.M., Melfi, A.J. (Eds.), The Mesozoic Flood Volcanism of the Paraná Basin. Petrogenetic and Geophysical Aspects. Universidade de São Paulo. Instituto Astronômico e Geofísico, São Paulo, pp. 47–72.

Comin-Chiaramonti, P., Cundari, A., Piccirillo, E.M., Gomes, C.B., Castorina, F., Censi, P., De Min, A., Marzoli, A., Speziale, S., Velázquez, V.F., 1997. Potassic and sodic igneous rocks from eastern Paraguay: their origin from the lithospheric mantle and genetic relationships with the associated Paraná flood tholeiites. J. Petrol. 38 (4), 495–528.

Comin-Chiaramonti, P., De Barros Gomes, C., Castorina, F., Di Censi, P., Antonini, P., Furtado, S., Ruberti, E., Scheibe, L.F., 2002. Geochemistry and geodynamic implications of the Anitápolis and Lages alkaline carbonatite complexes, Santa Catarina state, Brazil. Rev. Bras. Geosci. 32 (1), 43–58.

Comin-Chiaramonti, P., de Barros Gomes, C., Cundari, A., Castorina, F., Censi, P., 2007a. A review of carbonatitic magmatism in the Paraná-Angola-Namibia (PAN) system. Period. Miner. 76 (2-3), 25–78.

Comin-Chiaramonti, P., Marzoli, A., Gomes, C.B., Milan, A., Riccomini, C., Mantovani, M.M.S., Renne, P., Tassinari, C.C.G., Vasconcelos, P.M., 2007b. Origin of post Paleozoic magmatism in Eastern Paraguay. In: Foulger, G.R., Jurdy, D.M. (Eds.), Plates, Plumes, and Planetary Processes. The Geological Society of America Special Paper 430, Washington, D.C., pp. 603–633.

Comin-Chiaramonti, P., De Min, A., Girardi, V.A.V., Gomes, C.B., 2014. Carbonatites and primary carbonates in the Rio Apa and Amambay regions, NE Paraguay. Lithosphere 188, 84–96.

Cordani, U.G., Civetta, L., Mantovani, M.S.M., Petrini, R., Kawashita, K., Hawesworth, C.J., Taylor, P., Longinelli, A., Cavazini, G., Piccirillo, E.M., 1988. Isotope geochemistry of flood colcanics from the Paraná Basin. In: Piccirillo, E.M., Melfi, A.J. (Eds.), The Mesozoic Flood Volcanism of the Paraná Basin. Petrogenetic and Geophysical Aspects. Universidade de São Paulo. Instituto Astronômico e Geofísico, São Paulo, pp. 157–178.

Dasgupta, R., Mallik, A., Tsuno, K., Withers, A.C., Hirth, G., Hirschmann, M.M., 2013. Carbon-dioxide-rich silicate melt in the Earth's upper mantle. Nature 493, 211–215.

DePaolo, D.J., 1981a. Neodymium isotopes in the Colorado Front Range and crust-mantle evolution in the Proterozoic. Nature 291, 193–196.

DePaolo, D.J., 1981b. Trace elements and isotopic effects of combined Wallrock assimilation and fractional crystallization. Earth Planet. Sci. Lett. 53 (2), 189–202.

Ernesto, M., Marques, L.S., Piccirillo, E.M., Molina, E.C., Ussami, N., Comin-Chiaramonti, P., Bellieni, G., 2002. Paraná Magmatic Province-Tristan da Cunha plume system: fixed versus mobile plume, petrogenetic considerations and alternative heat sources. J. Volcanol. Geotherm. Res. 118, 15–36.

Ewart, A., Marsh, J.S., Milner, S.C., Duncan, A.R., Kamber, B.S., Armstrong, R.A., 2004. Petrology and geochemistry of Early Cretaceous bimodal continental flood volcanism of the NW Etendeka, Namibia. Part 1: introduction, mafic lavas and re-evaluation of mantle source components. J. Petrol. 45 (1), 59–105.

Florisbal, L.M., Bitencourt, M.F., Nardi, L.V.S., Conceição, R.V., 2009. Early post-collisional granitic and coeval mafic magmatism of medium- to high-K tholeiitic affinity within the Neoproterozoic Southern Brazilian Shear Belt. Precambrian Res. 175, 135–148.

Foulger, G.R., Natland, J.H., 2003. Is "Hotspot" volcanism a consequence of plate tectonics? Science 300, 921–922.

Gibson, S.A., Thompson, R.N., Dickin, A.P., Leonardos, O.H., 1995. High-Ti and low-Ti mafic potassic magmas: key to plume-lithosphere interactions and continental flood-basalt genesis. Earth Planet. Sci. Lett. 136, 149–165.

Gomes, C.B., Ruberti, E., Comin-Chiaramonti, P., Azzone, R.G., 2011. Alkaline magmatism in the Ponta Grossa Arch, SE Brazil: a review. J. S. Am. Earth Sci. 32, 152–168.

Gregory, T.R., Bitencourt, M.F., Nardi, L.V.S., Florisbal, L.M., Chemale Jr., F., 2015. Geochronological data from TTG-type rock associations of the Arroio dos Ratos Complex and implications for crustal evolution of southernmost Brazil in Paleoproterozoic times. J. S. Am. Earth Sci. 57, 49–60.

Guimarães, I.P., Da Silva Filho, A.F., Melo, S.C., Macambira, M.B., 2005. Petrogenesis of A-type Granitoids from the Alto Moxoto and Alto Pajeu Terranes of the Borborema Province, NE Brazil: Constraints from Geochemistry and Isotopic Composition. Gondwana Res. 8 (3), 347–362.

Harmon, R.S., Halliday, A.N., Clayburn, J.A.P., Stephens, W.E., 1984. Chemical and isotopic systematics of the Caledonian intrusions of Scotland and Northern England: a guide to magma source region and magma-crust interaction. Philos. Trans. R. Soc. Lond. 310, 709–742.

Hart, S.R., 1984. A large-scale isotope anomaly in the Southern Hemisphere mantle. Nature 309, 753–757.

Hawkesworth, C.J., Marsh, J.S., Duncan, A.R., Erlank, A.J., Norry, M.J., 1984. The role of continental lithosphere in the generation of the Karoo volcanic rocks: evidence from combined Nd- and Sr-isotope studies. In: Erlank, A.J. (Ed.), Petrogenesis of the Volcanic Rocks of the Karoo Province. Special Publication, Geological Society of South Africa. 13, pp. 341–354.

Hawkesworth, C.J., Mantovani, M.S.M., Peate, D.W., 1988. Lithosphere remobilization during Paraná magmatism. In: Menzies, M.A., Cox, K.G. (Eds.), Oceanic and Continental Lithosphere: Similarities and Differences. Journal of Petrology Special Volume, pp. 205–233.

Hill, E., Wood, B.J., Blundy, J.D., 2000. The effect of Ca-Tschermaks component on trace element partitioning between clinopyroxene and silicate melt. Lithos 53, 203–215.

Hirose, K., 1997. Partial melt compositions of carbonated peridotite at 3 GPa and role of CO_2 in alkali-basalt magma generation. Geophys. Res. Lett. 24 (22), 2837–2840.

Hirschmann, M.M., 2000. Mantle solidus: Experimental constraints and the effects of peridotite composition. Geochem. Geophys. Geosyst. 1 (10):1042. https://doi:10.1029/2000GC000070.

Hoernle, K., Rohde, J., Hauff, F., Garbe-Schönberg, D., Homrighausen, S., Werner, R., Morgan, J.P., 2015. How and when plume zonation appeared during the 132 Myr evolution of the Tristan Hotspot. Nat. Commun. 6, 7799.

Hofmann, A.W., 2003. Sampling mantle heterogeneity through oceanic basalts: Isotopes and trace elements. In: Holland, H.D., Turekian, K.K. (Eds.), Treatise on Geochemistry, the Mantle and Core. Elsevier, Oxford, pp. 61–101.

Huang, Y.-M., Hawkesworth, C.J., van Calsteren, P., McDermott, F., 1995. Geochemical characteristics and origin of the Jacupiranga carbonatites, Brazil. Chem. Geol. 119, 79–99.

Iacumin, M., De Min, A., Piccirillo, E.M., Bellieni, G., 2003. Source mantle heterogeneity and its role in the genesis of Late Archean-Proterozoic (2.7–1.0 Ga) and Mesozoic (200 and 130 Ma) tholeiitic magmatism in the South American Platform. Earth Sci. Rev. 62, 365–397.

Janasi, V.A., Freitas, V.A., Heaman, L.H., 2011. The onset of flood basalt volcanism, Northern Paraná Basin, Brazil: a precise U-Pb baddeleyite/zircon age for a Chapecó-type dacite. Earth Planet. Sci. Lett. 302, 147–153.

John, T., Klemd, R., Klemme, S., Pfänder, J.A., Hoffmann, J.E., Gao, J., 2011. Nb-Ta fractionation by partial melting at the titanite-rutile transition. Contrib. Mineral. Petrol. 161, 35–45.

Le Bas, M.J., Le Maitre, R.W., Streckeisen, A., Zanettin, B., 1986. A chemical classification of volcanic rocks based on the total alkali-silica diagram. J. Petrol. 27 (3), 745–750.

Mantovani, M.S.M., Peate, D.W., Hawkesworth, C.J., 1988. Geochemical stratigraphy of Paraná continental flood basalts: a contribution from borehole samples. In: Piccirillo, E.M., Melfi, A.J. (Eds.), The Mesozoic Flood Volcanism of the Paraná Basin. Petrogenetic and Geophysical Aspects. Universidade de São Paulo. Instituto Astronômico e Geofísico, São Paulo, pp. 15–24.

Mariani, P., Braitenberg, C., Ussami, N., 2013. Explaining the thick crust in Paraná basin, Brazil, with satellite GOCE gravity observations. J. S. Am. Earth Sci. 45, 209–223.

Marques, L.S., Dupré, B., Piccirillo, E.M., 1999. Mantle source compositions of the Paraná Magmatic Province (southern Brazil): evidence from trace element and Sr-Nd-Pb isotope geochemistry. J. Geodyn. 28, 439–458.

Marzoli, A., Melluso, L., Morra, V., Renne, P.R., Sgrosso, I., D'Antonio, M., Duarte Morais, L., Morais, E.A.A., Ricci, G., 1999. Geochronology and petrology of Cretaceous basaltic magmatism in the Kwanza basin (western Angola), and relationships with the Paraná-Etendeka continental flood basalt province. J. Geodyn. 28, 341–356.

Mattielli, N., Weis, D., Scoates, J.S., Shimizu, N., GréGoire, M., Mennessier, J.P., Cottin, J.Y., Giret, A., 1999. Evolution of heterogeneous lithospheric mantle in a plume environment beneath the Kerguelen Archipelago. J. Petrol. 40 (11), 1721–1744.

McDonough, W.F., Sun, S.-S., 1995. The composition of the Earth. Chem. Geol. 120, 223–253.

Melfi, A.J., Piccirillo, E.M., Nardy, A.J.R., 1988. Geological and magmatic aspects of the Paraná basin — an introduction. In: Piccirillo, E.M., Melfi, A.J. (Eds.), The Mesozoic Flood Volcanism of the Paraná Basin. Petrogenetic and Geophysical Aspects. Universidade de São Paulo. Instituto Astronômico e Geofísico, São Paulo, pp. 1–13.

Miyashiro, A., 1978. Nature of alkalic volcanic rocks series. Contrib. Mineral. Petrol. 66 (1), 91–104.

Navon, O., Stolper, E., 1987. Geochemical consequences of melt percolation: the upper mantle as a chromatographic column. J. Geol. 95 (3), 285–307.

Nwe, Y.Y., 1975. Two different pyroxene crystallization trends in the trough bands of the Skaergaard intrusion, East Greenland. Contrib. Mineral. Petrol. 49, 285–300.

Papike, J.J., Cameron, K.L., Baldwin, K., 1974. Amphiboles and Pyroxenes: Characterization of Other Than Quadrilateral Components and Estimates of Ferric Iron from Microprobe Data. Geological Society of America. Abstract with Program. 6 pp. 1053–1054.

Peate, D.W., 1997. The Paraná-Etendeka province. In: Mahoney, J.J., Coffin, M.F. (Eds.), Large Igneous Provinces: Continental, Oceanic, and Planetary Flood Volcanism. Geophysical Monograph. 100, pp. 217–246.

Peate, D.W., Hawkesworth, C.J., 1996. Litospheric to astenospheric transition in Low-Ti flood basalts from southern Paraná, Brazil. Chem. Geol. 127, 1–24.

Peate, D.W., Mantovani, M.S.M., Hawkesworth, C.J., 1988. Geochemical stratigraphy of the Paraná continental flood basalts: borehole evidence. Rev. Bras. Geosci. 18 (2), 212–221.

Peate, D.W., Hawkesworth, C.J., Mantovani, M.S.M., 1992. Chemical stratigraphy of the Paraná lavas (South America): classification of magma types and their spatial distribution. Bull. Volcanol. 55, 119–139.

Peate, D.W., Hawkesworth, C.J., Mantovani, M.S.M., Rogers, N.W., Turner, S.P., 1999. Petrogenesis and stratigraphy of the High-Ti/Y Urubici magma type in the Paraná flood basalt province and implications for the nature of "Dupal"-type mantle in the South Atlantic region. J. Petrol. 40 (3), 451–473.

Piccirillo, E.M., Melfi, A.J., 1988. The Mesozoic flood Volcanism of the Paraná Basin. Petrogenetic and Geophysical Aspects. Universidade de São Paulo. Instituto Astrônomico e Geofísico.

Piccirillo, E.M., Melfi, A.J., Comin-Chiaramonti, P., Bellieni, G., Ernesto, M., Marques, L.S., Nardy, A.J.R., Pacca, I.G., Roisenberg, A., Stolfa, D., 1988. Continental Flood Volcanism from the Paraná Basin (Brazil). In: Macdougall, J.D. (Ed.), Continental Flood Basalts. Kluwer Academic Publishers, Dordrecht, pp. 195–238.

Piccirillo, E.M., Civetta, L., Petrini, R., Longinelli, A., Bellieni, G., Comin-Chiaramonti, P., Marques, L.S., Melfi, A.J., 1989. Regional variations within the Paraná flood basalts (southern Brazil): evidence for subcontinental mantle heterogeneity and crustal contamination. Chem. Geol. 75, 103–122.

Piccirillo, E.M., Bellieni, G., Cavazzini, G., Comin-Chiaramonti, P., Petrini, R., Melfi, A.J., Pinese, J.P.P., Zantadeschi, P., De Min, A., 1990. Lower Cretaceous tholeiitic dyke swarms from the Ponta Grossa Arch (southeast Brazil): petrology, Sr-Nd isotopes and genetic relationships with the Paraná flood volcanics. Chem. Geol. 89, 19–48.

Pin, C., Briot, D., Bassin, C., Poitrasson, F., 1994. Concomitant separation of strontium and samarium neodymium for isotopic analysis in silicate samples, based on specific extraction chromatography. Anal. Chim. Acta 298 (2), 209–217.

Renne, P.R., Ernesto, M., Pacca, I.G., Coe, R.S., Glen, J.M., Prévot, M., Perrin, M., 1992. The age of Paraná flood volcanism, rifting of Gondwanaland, and the Jurassic-Cretaceous boundary. Science 258, 975–979.

Renne, P.R., Deckart, K., Ernesto, M., Féraud, G., Piccirillo, E.M., 1996. Age of the Ponta Grossa dike swarm (Brazil), and implications to Paraná flood volcanism. Earth Planet. Sci. Lett. 144, 199–211.

Renne, P.R., Mundil, R., Balco, G., Min, K., Ludwig, K.R., 2010. Joint determination of ^{40}K decay constants and $^{40}Ar^*/^{40}K$ for the Fish Canyon sanidine standard, and improved accuracy for $^{40}Ar/^{39}Ar$ geochronology. Geochim. Cosmochim. Acta 74, 5349–5367.

Renne, P.R., Balco, G., Ludwig, K.R., Mundil, R., Min, K., 2011. Response to the comment by W.H. Schwarz et al. on "Joint determination of ^{40}K decay constants and $^{40}Ar^*/^{40}K$ for the Fish Canyon sanidine standard, and improved accuracy for $^{40}Ar/^{39}Ar$ geochronology" by P.R. Renne et al. (2010). Geochim. Cosmochim. Acta 75, 5097–5100.

Rocha-Júnior, E.R.V., Puchtel, I.S., Marques, L.S., Walker, R.J., Machado, F.B., Nardy, A.J.R., Babinski, M., Figueiredo, A.M.G., 2012. Re-Os isotope and highly siderophile element systematics of the Paraná continental flood basalts (Brazil). Earth Planet. Sci. Lett. 337–338, 164–173.

Rocha-Júnior, E.R.V., Marques, L.S., Babinski, M., Nardy, A.J.R., Figueiredo, A.M.G., Machado, F.B., 2013. Sr-Nd-Pb isotopic constraints on the nature of the mantle sources involved in the genesis of the high-Ti tholeiites from northern Paraná Continental Flood Basalts (Brazil). J. S. Am. Earth Sci. 46, 9–25.

Rosset, A., De Min, A., Marques, L.S., Macambira, M.J.B., Ernesto, M., Renne, P.R., Piccirillo, E.M., 2007. Genesis and geodynamic significance of Mesoproterozoic and Early Cretaceous tholeiitic dyke swarms from the São Francisco craton (Brazil). J. S. Am. Earth Sci. 24, 69–92.

Rudnick, R.L., Gao, S., 2003. The composition of the continental crust. In: Rudnick, R.L., Holland, H.D., Turekian, K.K. (Eds.), The Crust, Volume 3, Treatise on Geochemistry. Elsevier-Pergamon, Oxford, pp. 1–64.

da Silva, L.C., McNaughton, N.J., Armstrong, R., Hartmann, L.A., Fletcher, I.R., 2005. The neoproterozoic Mantiqueira Province and its African connections: a zircon-based U-Pb geochronologic subdivision for the Brasiliano/Pan-African systems of orogens. Precambrian Res. 136, 203–240.

Steinberger, B., Torsvik, T.H., 2012. A geodynamic model of plumes from the margins of Large Low Shear Velocity Provinces. Geochem. Geophys. Geosyst. 13 (1). http://dx.doi.org/10.1029/2011GC003808.

Sun, S.-S., McDonough, W.F., 1989. Chemical and isotopic systematics of oceanic basalts: implications for mantle composition and processes. In: Saunders, A.D., Norry, M.J. (Eds.), Magmatism in the Ocean Basins. 42. Geological Society of London, Special Publication, London, pp. 313–345.

Tanaka, T., Togashi, S., Kamioka, H., Amakawa, H., Kagami, H., Hamamoto, T., Yuhra, M., Orihashi, J., Yoneda, S., Shimizu, H., Kunimaru, T., Takahashi, K., Yanagi, T., Nakano, T., Fujimaki, H., Shinjo, R., Asahara, Y., Taminizu, M., Dragusanu, C., 2000. JNdi-1: a neodymium isotopic reference in consistency with LaJolla neodymium. Chem. Geol. 168 (3), 279–281.

Tappe, S., Foley, S.F., Jenner, G.A., Heaman, L.M., Kjarsgaard, B.A., Romer, R.L., Stracke, A., Joyce, N., Hoefs, J., 2006. Genesis of ultramafic lamprophyres and carbonatites at Aillik Bay, Labrador: a consequence of incipient lithospheric thinning beneath the North Atlantic Craton. J. Petrol. 47 (7), 1261–1315.

Thiede, D.S., Vasconcelos, P.M., 2010. Paraná flood basalts: rapid extrusion hypothesis confirmed by new $^{40}Ar/^{39}Ar$ results. Geology 38 (8), 747–750.

Till, C.B., Tanton, L.T.E., Fischer, K.M., 2010. A mechanism for low - extent melts at the lithosphere - asthenosphere boundary. Geochem. Geophys. Geosyst. 11. http://dx.doi.org/10.1029/2010GC003234.

Turner, S., Hawkesworth, C., Gallagher, K., Stewart, K., Peate, D., Mantovani, M., 1996. Mantle plumes, flood basalts, and thermal models for melt generation beneath continents: assessment of a conductive heating model and application to the Paraná. J. Geophys. Res. 101, 11503–11518.

Vidotti, R.M., Ebinger, C.J., Fairhead, J.D., 1998. Gravity signature of the western Paraná basin, Brazil. Earth Planet. Sci. Lett. 159, 117–132.

Weaver, B.L., Wood, D.A., Tarney, J., Joron, J.L., 1987. Geochemistry of ocean island basalts from the South Atlantic: Ascension, Bouvet, St. Helena, Gough and Tristan da Cunha. Geological Society, London, Spec. Publ. 30, pp. 253-267.

Weit, A., Trumbull, R.B., Keiding, J.K., Geissler, W.H., Gibson, S.A., Veksler, I.V., 2016. The magmatic system beneath the Tristan da Cunha island: insights from thermobarometry, melting models and geophysics. Tectonophysics http://dx.doi.org/10.1016/j.tecto.2016.08.010.

Wyllie, P.J., 1989. Origin of carbonatites: evidence from phase equilibrium studies. In: Bell, K. (Ed.), Carbonatites: Genesis and Evolution. Unwin Hyman, London, pp. 500–545.

Zindler, A., Hart, S., 1986. Chemical geodynamics. Annu. Rev. Earth Planet. Sci. 14, 493–571.